Article

Not peer-reviewed version

Power Control of PV Generation, Electric Mobility, Electric Heating and Battery Energy Storage

Nikolaos Damianakis *, Gautham Ram Chandra-Mouli, Pavol Bauer

Posted Date: 16 June 2026

doi: 10.20944/preprints202606.1277.v1

Keywords: battery energy storage; degradation; electric vehicles; heat pumps; MIQP; power control; PVs

Article

Power Control of PV Generation, Electric Mobility, Electric Heating and Battery Energy Storage

Nikolaos Damianakis *, Gautham Ram Chandra-Mouli and Pavol Bauer

Department of Electrical Sustainable Energy, Faculty of Electrical Engineering, Mathematics, and Computer Science, Technische Universiteit Delft (TU Delft), Mekelweg 4, 2628 CD Delft, The Netherlands
* Correspondence: n.damianakis@tudelft.nl

Abstract

Power control of photovoltaic generation, flexible loads, e.g. electric vehicles and heat pumps, and battery energy storage systems (BESS) have become important for energy arbitrage. This work develops a two-level power control model for day-ahead and real-time scheduling, where the contribution of flexible loads (e.g. vehicle-to-grid (V2G) use) and BESS is compared, considering different grid types, grid sizes, seasons, and battery degradation. An empirical degradation model has been linearized and incorporated, including cyclic and calendar aging. The results showed that the seasonal effect significantly influences the grid power exchange and the V2G use. Moreover, the grid type has a notable impact on the flexibility of the node since commercial grids import less grid power and use less V2G due to lower flexibility. Furthermore, a larger grid size decreases the need for BESS use and increases the likelihood of V2G use. While degradation has a small effect on the total cost of small grids, the effect increases notably as the size of the grid increases, while it also greatly reduces V2G and BESS use. Finally, the model has been validated against benchmark and control models, showing cost reductions of up to 5.81% and 30.6%, without and with BESS use, respectively.

Keywords: battery energy storage; degradation; electric vehicles; heat pumps; MIQP; power control; PVs

---

1. Introduction

Electric mobility and heating with electric vehicles (EVs) and heat pumps (HPs), respectively, will play a huge role in the energy transition since transportation and heating constitute major contributors to carbon emissions [1,2]. For example, a recent analysis published by Eurostat [3] showed that 40% of the total carbon emissions in Europe in 2022 are caused by the transportation (26.2%) and building sectors (13.8% for residential and commercial buildings). However, uncontrolled adoption of EVs and HPs can cause several grid impact issues, such as overloading, voltage violations, peak demands, etc. [4]. Moreover, a high penetration of renewable energy sources (RESs) is expected, such as distributed energy resources (DERs) and photovoltaics (PVs). However, rapid PV output fluctuations can further jeopardize power quality in future distribution grids (DGs), e.g. provoking voltage unbalance, flickering, etc. [5].

Therefore, on the one hand, power control of PVs, flexible loads such as EVs and HPs, and (battery) energy storage systems ((B)ESSs) in energy management systems (EMSs) will become necessary in future low voltage (LV) DGs with the aim of energy arbitrage with minimum cost, PV self-consumption increase and avoiding grid violations [6,7]. Demand side management (DSM) concepts have emerged to assist in the power scheduling of EMSs performing load shifting, load shedding, etc. [8]. On the other hand, ancillary services such as frequency regulation or congestion management can be provided to the power grid [9,10]. In this regard, the vehicle-to-grid (V2G) capability of the EVs can also provide significant support, transforming the EVs into mobile ESSs [11]. Such EMSs have been developed on a household level, e.g., home energy management systems (HEMSs) [12], or grid level, usually using aggregators [7]. Additionally, several uncertainties are present in power control, which can affect the objectives of the EMSs, such as the intermittent supply of PV power, weather conditions, energy prices, EV driving patterns, etc. [1,13]. Therefore, EMSs specialized in dealing with uncertainties have been developed following stochastic, robust, and model-predictive-control (MPC) approaches, such as in [14–16].

Several power control systems (PCSs) exist in the literature that exploit the flexibility of low-carbon technologies (LCTs), such as PVs, EVs, HPs, and ESSs, with various objectives and demand response (DR) strategies, such as energy arbitrage, peak shaving, voltage control, frequency regulation, congestion management and other ancillary services provision. Due to the scope of this work, the next section is devoted to the review of such existing ESS-integrated PCSs in the literature.

2. Literature Review & Contributions

2.1. Reviewed Power Control Studies

ESS, PVs, and EVs with V2G capability were integrated into the rule-based HEMS of [17] and tested under different price mechanisms. Furthermore, uncertainties present in power control, such as EV driving patterns, weather conditions, and energy prices, were effectively managed in the 2-stage stochastic dynamic approach in [14]. A goal programming approach was followed in [18] for the energy management of a smart building equipped with PVs, EVs, and BESS, while different DR programs were implemented in the developed residential HEMS of [19], which achieved a reduction of electricity cost and peak-to-average ratio by 25.55% and 36.98%, respectively. However, all of these EMSs remained on a home- or building-level (H/BEMSs). Regarding grid-level studies, a district EMS that managed RES, ESS, and EVs was formulated in [20] and solved deterministically and stochastically to reveal the effect of uncertainties in power control. Voltage management was provided by the same LCTs in the multi-agent DG in [21], while the flexibility provided by regenerative braking energy combined with PVs and ESSs was studied for the integrated rail system and EV parking lot in [22]. In [16,23], the authors also considered the effect of battery degradation, where centralized and decentralized strategies were compared concerning the EMS performance. Moreover, battery degradation was also accounted for in the studies of [24,25], which investigated the potential of the PV-EV-ESS cooperation for ancillary services provision. Finally, an optimal sizing and control study considering lifetime cost and performance analysis can be found in [11]. However, none of the above ESS-integrated studies exploited the flexibility of HPs in their investigations.

Regarding HP integration in ESS-integrated studies, PVs, HPs, and ESS were combined in the MPC BEMSs of [26,27] for energy arbitrage, showing significant cost savings, while different ESS control strategies for self-consumption increase were studied in [28]. HPs and thermal ESS (TESS)/BESS were coupled using DSM strategies for peak reduction and uncertainty management in the district-level studies of [29,30] and the grid-level study of [31], where different energy demands were considered for residential, commercial, and industrial areas. PVs were also integrated into the EMSs of [32] and of a virtual power plant comprising 67 dwellings in [8], while their contribution to ancillary services provision in multi-energy communities respecting the thermal comfort of the residents was shown in [33]. The synergy of thermal and electrical storage was also considered in [15,34], showing the benefits of their coupling in multi-carrier microgrids when scheduling under uncertainties. However, EVs were not accounted for in all of the above HP/ESS-integrated investigations.

A PCS that controls PVs, EVs, HPs, and a TESS was developed on [35], where the authors compared rule-based and MPC techniques considering cost, carbon-, and flexibility-oriented objectives. Multi-objective HEMS and BEMS were developed in [36,37], respectively, which control PVs, EVs, HPs, BESS, and non-flexible loads. Considered objectives were the total cost, thermal and habit discomfort, EV range anxiety discomfort, max PV self-consumption, etc. However, the battery degradation effect was ignored in these studies. On the contrary, an optimal trade-off between energy and battery degradation costs was searched in the MPC study in [38], but the seasonal effect was not considered. Finally, both seasonal and degradation effects, as well as uncertainty management, were incorporated

 doi:10.20944/preprints202606.1277.v1

in the 2-stage model in [39], showing that BESS and EV degradation costs are not negligible compared to the total energy cost. Finally, two PV-EV-HP-BESS BEMSs can be found in [40,41], showing the effect of the energy price and peak demand tariffs on the power control and the importance of adaptation of the MPC models according to uncertain variable deviations, respectively.

Nevertheless, while the studies in [35–41] considered PVs, EVs, HPs, and ESS solutions, they all remained on a home- or building-level. Such an investigation was conducted in the multi-objective robust work in [42], where the cooperative optimization of three integrated energy systems was found via a Nash bargaining problem. However, consideration of V2G was left out of the study. A smart-grid analysis that comprised PVs, HPs, EVs, and TESS can be found in [44], which showed that a coupled control system could effectively improve PV self-consumption by 77%. However, the degradation effect was ignored while the study remained on a microgrid level comprising 3 buildings. Additionally, a grid-level analysis was conducted in [43], which studied a robust EMS against uncertainties and various uncertainty budgets. However, various effects such as the seasonal, degradation, and grid size effects were not incorporated in the study.

2.2. Contributions

Table 1 summarizes the reviewed ESS-integrated power control studies. Because this work develops a grid-level PCS, and the grid size is very important to its findings, only grid-level studies are integrated in Table 1. Firstly, a grid-level power control work that comprises PVs, EVs, HPs, and ESS, and considers multiple influencing factors (e.g. different grid types, grid sizes, and seasons) for energy arbitrage without grid violations is missing. Secondly, comparing the flexibility of ESSs and flexible loads (e.g. V2G-capable EVs) in an EMS has not been investigated in studies that consider all the above LCTs. Thirdly, the effect of battery degradation on power scheduling has not yet been investigated in such grid-level power control studies. However, the consideration of battery degradation is especially important in grid-level studies that perform energy arbitrage, since the accumulated degradation costs from the BESS and the multiple EV batteries can result in comparable numbers to the total power control cost. Therefore, a two-level mixed-integer quadratic programming (MIQP) model for both day-ahead (DA) and real-time (RT) scheduling of PVs, EVs, HPs, and BESS has been developed and tested under different seasons and grid scenarios. The contributions of the work can be summarized as follows:

1) Develops a two-level MIQP power control of PV generation, EVs, HPs, and BESS, and investigates the contribution of BESSs and flexible loads, such as V2G, to energy arbitrage without grid violations, which has not yet been investigated in earlier works.

2) Applies the power control for day-ahead scheduling and real-time scheduling with uncertainty management, investigating the influence of different seasons, grid types (residential, commercial), small and large grid sizes, and battery degradation, which is still missing from the existing literature.

3) Develops and integrates a linearized battery degradation model into the power control, which is based on a physics-guided semi-empirical battery degradation model that accounts for calendar and cyclic aging and considers various degradation influencing factors, such as time, temperature, C-rate, throughput, etc. The developed linearized battery degradation model is effectively incorporated into the power control, achieving high accuracy with significantly lower computational burden than the original highly non-linear semi-empirical model. According to the authors' knowledge, this has not yet been done in the existing MILP/MIQP grid-level power control works in the literature.

To highlight more the contribution of this work, the integration of PVs, V2G-capable EVs, HPs, and BESS has not yet been investigated in multiple grid-level studies, because the greatest challenge is to encompass and optimize all the LCTs with reasonable accuracy and computational time, and provide proof that the PCS model can work effectively even when the testing grid size increases. In this work, the PCS managed to consider multiple modeling details that are often ignored in the literature and still remained MIQP to be solvable in a reasonable computational time.

The rest of the work is categorized as follows: Sections 3 and 4 comprise the concept and modeling of power control, respectively, while Section 5 integrates the utilized case studies and scenarios. Results

Preprints.org (www.preprints.org) | NOT PEER-REVIEWED | Posted: 16 June 2026 doi:10.20944/preprints202606.1277.v1

are summarized in Section 6, while Section 7 integrates the discussion and validation. Finally, Section 8 concludes the work.

Table 1. Characteristics & Contributions of Grid-level ESS-integrated Power Control Studies .

Ref	PVs	EVs	V2G	HPs	Battery Aging	ESSs / Loads	Seasons	Grid Size	Grid Type
[29]				✓			✓		
[31]				✓			✓	✓	✓
[34]	✓			✓					
[30]	✓			✓			✓		
[32]	✓			✓					✓
[15]	✓			✓	✓				
[33]	✓			✓		✓	✓		
[8]	✓			✓		✓	✓		
[21]	✓	✓							
[16]	✓	✓			✓				
[22]	✓	✓				✓			
[24]	✓	✓			✓				
[20]	✓	✓	✓						
[23]	✓	✓	✓		✓				
[25]	✓	✓	✓		✓				
[11]	✓	✓	✓		✓		✓		
[42]	✓	✓		✓				✓	✓
[43]	✓	✓	✓	✓					
[44]	✓	✓	✓	✓			✓		
Work	✓	✓	✓	✓	✓	✓	✓	✓	✓

3. Power Control Concept

The PCS aims to exploit in both levels the flexibility of the flexible loads (HPs and V2G-capable EVs) and BESS to perform energy arbitrage, minimizing PV curtailment, satisfying the charging and thermal comfort of the customers, and avoiding grid violations. It is formulated as a decentralized node optimization; thus, all grid nodes are optimized simultaneously and independently. In this work, a "node" means an aggregation of buildings equipped with PV rooftops and HPs, EV chargers, and a BESS (one BESS per node). EVs that are connected to the EV chargers participate in the power control after their state-of-charge (SOC) surpasses a predefined threshold; in this work, assumed to be 20%. The authors believe that it would be a very important limitation if the PCS was centralized. Hence, every further re-optimization trigger due to a larger set of EVs or buildings would substantially increase the computational expense. On the contrary, the developed PCS is decentralized and optimizes every node distributionally by initially setting their power limit setpoints (division of the grid capacity). In that way, the PCS is less affected by large grid sizes with thousands of loads.

The power control uses two optimization levels, which are described in Figure 1 (a). The first level is used for DA scheduling, and it is a one-shot (single) optimization of the next day. It uses forecast data about the EV driving patterns (e.g., requested energy, arrival SOC, arrival and departure time, etc.) and the buildings' occupancy for the power control of the EVs and HPs, respectively. It is triggered at the start of the day (00:00), and besides providing an estimated power scheduling for the next day, it can be used in future work for other purposes, such as bidding in the wholesale reserve market for

doi:10.20944/preprints202606.1277.v1

ancillary services provision. The second level is used for RT power scheduling, and it is formulated as an MPC problem that uses rolling-horizon optimization (RHO) and triggers re-optimizations upon certain events. This level initially uses predicted data about the EV driving patterns and buildings' occupancy to control the horizon and replaces them with actual data when the EVs finally arrive, and the buildings are (dis-)occupied, respectively.

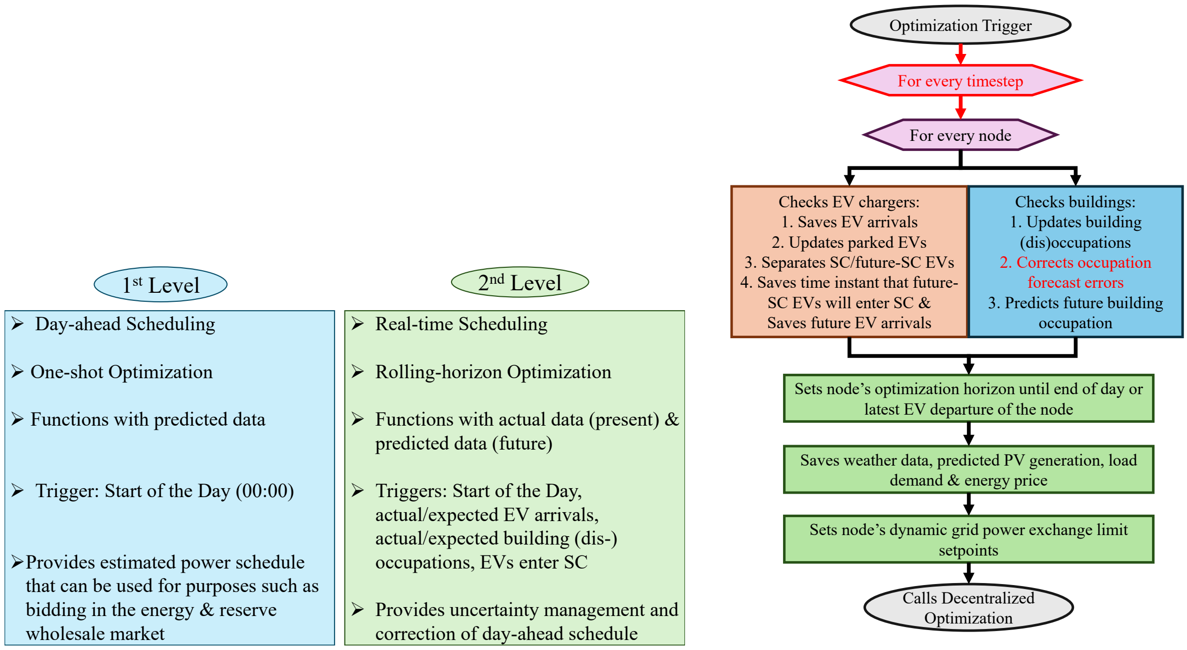

(a) (b)

Figure 1. Description of the PCS concept: (**a**)Characteristics of the optimization levels of the PCS. (**b**) Flowchart of the PCS optimization levels.

Re-optimizations are triggered upon the events: start of the day (00:00), new/expected EV arrivals, EV participation in power control ($SOC > 20\%$), and new/expected building occupancy changes. Finally, Level 2 can also be used for ancillary services provision, such as deploying offered frequency regulation reserves or congestion management. For a realistic PCS simulation, if historical data is not available for the estimated DA schedule, we assume a direct information feed between the customers and the PCS the day before. Triggering re-optimizations, the RHO of Level 2 provides uncertainty management and corrects forecast errors from the estimated DA schedule. The effectiveness of this concept has been demonstrated by inserting a level of uncertainty in all optimization triggers between the expected and the actual profiles using a normal distribution with 0′ mean and 15′ max deviation. The PCS has been successful in achieving its objectives (EV charging, building cooling/heating, PV curtailment minimization) at both levels. Hence, using a bi-level formulation can provide uncertainty management.

The flowchart of the power control model is depicted in Figure 1 (b). All depicted control steps apply for both levels except for the red-colored ones that apply only for the RT scheduling (Level 2). Every node is checked at every timestep for optimization triggers. When an optimization is triggered, all EV chargers are checked for new EV arrivals, and the dynamic charging characteristics of every parked EV are updated. Additionally, the EVs that have $SOC > 20\%$ and participate immediately in the power control (SC EVs) are separated from the EVs that will participate in the future (future-SC EVs). Thereafter, the estimated control participation time of the future-SC EVs and the predicted future EV arrivals in the chargers are saved. Simultaneously, the current occupation of every building is checked, while the future dynamic building occupation is also stored. Afterward, the optimization horizon in both layers is set until the end of the day or the latest EV departure between the EVs still connected at the end of the day. The forecast data needed for the power control, such as weather data, PV generation, load demand, energy price, etc.) during the optimization horizon is saved, and the dynamic grid power exchange limit setpoints are set for every node. All nodes share a total power capacity for grid power exchange, which is divided among the nodes according to the consumption level of their assets and is consequently used as a setpoint for imported and exported grid power. Finally, the decentralized optimization is called for the nodes with optimization triggers.

4. Power Control Modeling

The developed MIQP PCS model is categorized into BESS/EV, building, node, and degradation constraints. The model constitutes an extension of the MILP problem in [45] and uses a timestep $\Delta t = 5'$ to maintain an efficient trade-off between accuracy and computational expense. The utilized indices $n, j, b, bes, t, T, ch, dis, init, end$ represent the node, charger, building, BESS, time instant, optimization horizon, charging, and discharging, initial, and final, respectively. All equations apply for $\forall t \in T$ unless stated otherwise.

4.1. Battery Energy Storage & EV Constraints

The EV and BESS constraints of the power control model are listed below, where the indices a, d represent the arrival and departure, respectively. The BESS modeled represents a lithium ferrophosphate battery (LFP).

$$P_{ch/dis}^{n,j/bes,t} = \Phi^{n,j} I_{ch/dis}^{n,j/bes,t} V^{n,t} \tag{1}$$

$$0 \leq P_{ch/dis}^{n,j/bes,t} \leq P_{ch/dis_{max}}^{n,j/bes} \;\&\; 0 \leq I_{ch/dis}^{n,j/bes,t} \leq I_{ch/dis_{max}}^{n,j/bes} \tag{2}$$

Equation (1) dictates the dynamic EV and BESS charging $P_{ch}^{n,j/bes,t}$ and discharging $P_{dis}^{n,j/bes,t}$ powers where $I_{ch}^{n,j/bes,t}$ and $I_{dis}^{n,j/bes,t}$ the instantaneous phase charging and discharging currents, $\Phi^{n,j} = 3$ the number of used phases, and $V^{n,t} = V_{nom}$ the node voltage assumed steady at the nominal 230V. The limits of charging and discharging power and current are dictated in (2), which depend on the rated LCT specifications, e.g. according to most commercial V2G chargers [1] (see Table 2).

$$B^{n,j/bes,t} = B_{init}^{n,j/bes} + \Delta t \sum_{t_{init}}^{t} (P_{ch}^{n,j/bes,t} - P_{dis}^{n,j/bes,t}) \tag{3}$$

$$\begin{gathered} S^{n,j/bes,t} = B^{n,j/bes,t} / B_r^{n,j/bes} \\ S_{low}^{n,bes} \leq S^{n,bes,t} \leq S_{high}^{n,bes} \end{gathered} \tag{4}$$

$$I_{ch}^{n,j,t}, I_{dis}^{n,j,t}, B^{n,j,t} = 0 \;\; \forall t \notin [T_a^{n,j}, T_d^{n,j}] \tag{5}$$

The EV/BESS battery capacity dynamics $B^{n,j/bes,t}$ at every timestep Δt are modeled in (3) where $B_{init}^{n,j/bes}$ the initial battery capacity, equal to the arrival $B_a^{n,j}$ for EVs and 50% for the BESS. The EV/BESS SOC dynamics $S^{n,j/bes,t}$ are modeled in (4), which depend on the dynamic and rated battery capacity $B_r^{n,j/bes}$ of the BESS and EVs. The BESS SOC is always limited in a selected interval $[S_{low}^{n,bes}, S_{high}^{n,bes}]$ to prevent accelerated aging at very low and very high SOCs. On the contrary, all variables turn to zero in (5) for the EVs outside of the EV parking time $[T_a^{n,j}, T_d^{n,j}]$.

$$P_{ch}^{n,j/bes,t} \leq \left(\frac{S^{n,j/bes,t}}{k} + \frac{\alpha k - \beta}{\alpha k}\right) P_{ch_{max}}^{n,j/bes} : \alpha = 10, \beta = 9, k = 16 \tag{6}$$

$$\begin{gathered} I_{cv_{max,ch}}^{n,j/bes,t} = -\gamma I_r^{n,j/bes,t} S^{n,j/bes,t} + \gamma I_r^{n,j/bes,t} \\ I_{ch}^{n,j/bes,t} \leq I_{cv_{max,ch}}^{n,j/bes,t} \; : \; \gamma = 10 \end{gathered} \tag{7}$$

[1] https://fermataenergy.com/

 doi:10.20944/preprints202606.1277.v1

$$I_{cv_{max,dis}}^{n,j/bes,t} = \gamma I_r^{n,j/bes,t} S^{n,j/bes,t}$$
$$I_{dis}^{n,j/bes,t} \leq I_{cv_{max,dis}}^{n,j/bes,t} \,:\, \gamma = 10 \tag{8}$$

Equations (6)–(8) model a linear approximation of the Constant-Current - Constant-Voltage (CC-CV) BESS/EV charging/discharging region, derived by [9]. According to (6) and (7), the EVs and BESS are charged with linearly increasing power up to $SOC = 90\%$, where the charging power reaches its peak value, and consequently, the power decreases linearly to zero when SOC reaches 100%. The CV discharging region has also been considered in (8), according to which the power increases linearly to 100% when $SOC = [0\%, 10\%]$, and consequently the EVs and BESS provide maximum discharging power at $SOC = [10\%, 100\%]$. The variables $I_{cv_{max,dis}}^{n,j/bes,t}, I_{cv_{max,ch}}^{n,j/bes,t}$ are utilized to limit the EV and BESS discharging and charging power, respectively, during their respective SOC intervals, and they depend on the rated EV and BESS currents $I_r^{n,j/bes,t}$ and the dynamic SOCs $S^{n,j/bes,t}$. Parameters α, β, γ, k have been chosen as shown to create the slopes of the explained linear approximations, but can be moderated to create steeper or flatter slopes.

Table 2. BESS and EV Parameters of Coordinated Power Control Model.

Par.	Explanation	Value
$C_{ev_{pen}}^{n,j}$	EV Charg. Penalty	10€/(1%SOC)
$h_{ch}^{n,j}$	EV Charg. Efficiency	0.95
h_{bes}^{n}	BESS efficiency	0.98
$P_{ch_{max}}^{n,j}$	Max EV Charg. Power	$\min(P_{ev_r}^{n,j}, 22kW)$
$P_{dis_{max}}^{n,j}$	Max EV Disch. Power	$\min(P_{ev_r}^{n,j}, 20kW)$
$P_{ch/dis_{max}}^{n,bes}$	Max BESS (dis)charging Power	0.5C
$B_{init}^{n,bes}$	BESS Initial Capacity	$0.5B_r^{n,bes}$
$V^{n,t}$	Node Voltage	230V
$\Phi^{n,j/bes}$	Number of Phases	3
$I_{ch_{max}}^{n,j}$	Max EV Charg. Current	$\min(I_{ev_r}^{n,j}, 32A)$
$I_{dis_{max}}^{n,j}$	Max EV Disch. Current	$\min(I_{ev_r}^{n,j}, 29A)$
$S_{low}^{n,bes}$	Min BESS SOC	10%
$S_{high}^{n,bes}$	Max BESS SOC	90%
V_{nom}	Nominal Node Voltage	230V
$\mu_{min/max}^{bes}$	Min-Max BESS Capacity Thresholds	0.95, 1.05

$$b_{ch}^{n,j/bes,t} + b_{dis}^{n,j/bes,t} \leq 1 \;\; \forall t \in T \tag{9}$$

$$P_{ch}^{n,j/bes,t} \leq b_{ch}^{n,j/bes,t} P_{ch_{max}}^{n,j/bes} \;\; \forall t \in T \tag{10}$$

$$P_{dis}^{n,j/bes,t} \leq b_{dis}^{n,j/bes,t} P_{dis_{max}}^{n,j/bes} \;\; \forall t \in T \tag{11}$$

Equations (9)–(11) dictate that charging power P_{ch} and discharging power P_{dis} cannot be realized simultaneously. Binary variables $b_{ch}^{n,j,t}$ & $b_{v2g}^{n,j,t}$ are introduced and correlated to charging and discharging power, respectively, to activate only one mode at a time.

 doi:10.20944/preprints202606.1277.v1

$$E_g^{n,j} = B_a^{n,j} + d^{n,j} - B_d^{n,j} \tag{12}$$

$$B_{end}^{n,bes} \geq \mu_{min}^{bes} B_{init}^{n,bes} \ \& \ B_{end}^{n,bes} \leq \mu_{max}^{bes} B_{init}^{n,bes} \tag{13}$$

Moreover, (12) dictates the EV unfinished charging gap $E_g^{n,j}$ which is calculated by subtraction of the departure capacity $B_d^{n,j}$ from the sum of the arrival capacity $B_a^{n,j}$ and the requested energy $d^{n,j}$. This gap induces penalty costs for the PCS to be paid to the EV owners and is incorporated in the cost minimization of the objective function. Finally, (13) forces the final stored BESS energy $B_{end}^{n,bes}$ to remain at similar levels with the initial stored energy $B_{init}^{n,bes}$ with an accuracy error that depends on the $\mu_{min}^{bes}, \mu_{max}^{bes} = 5\%$ capacity thresholds, to omit the influence of the initial BESS SOC because of the daily simulation period.

4.2. Building Constraints

The constraints of the power control model concerning the PV generation and HP heating/cooling of the buildings are listed below, derived by [4,46], where: $surf, irr, sp, dhw, tank$ denote the surface, irradiation, space, domestic hot water (DHW), and tank, respectively. All constraints apply for $\forall t \in T$.

$$V_{tank} = V_{w_p} N_p f_{dhw} \tag{14}$$

$$A_{tank} = 2\pi R_{tank} H_{tank} + 2\pi R_{tank}^2 \tag{15}$$

$$T_{dhw}^{n,b,t} = T_{dhw_{init}}^{n,b} + \Delta t \sum_{t_{st}}^{t} \frac{(Q_{hp_{dhw}} - Q_{los_{dhw}})^{n,b,t}}{V_{tank} C_{wat} \rho_{wat}} \tag{16}$$

$$Q_{los_{dhw}}^{n,b,t} = U_{tank} A_{tank} (T_{dhw}^{n,b,t} - T_{sp}^{n,b,t}) \tag{17}$$

$$T_{dhw}^{n,b,t_{dhw}} = T_{dhw}^{des} \tag{18}$$

Regarding the DHW, the total volume V_{tank} and surface area A_{tank} of the DHW tank are modeled in (14) and (15) where $N_p, V_{w_p}, R_{tank}, H_{tank}$ the number of people in the building, the estimated water volume per person, the tank radius and the tank height, respectively. The DHW factor f_{dhw} has been set at 1.25 to provide a 25% extra tolerance for higher DHW use. The DHW temperature dynamics $T_{dhw}^{n,b,t}$ are dictated in (16), which depend on the heating gains from the HP operation $Q_{hp_{dhw}}$ and heating losses $Q_{los_{dhw}}$ divided by the total thermal capacity of the tank water where $T_{dhw_{init}}^{n,b}$ the initial DHW tank temperature, C_{wat} the water specific heating capacity and ρ_{wat} the water density. The tank heating losses are modeled in (17) and depend on the difference between the tank temperature $T_{dhw}^{n,b,t}$ and the building temperature $T_{sp}^{n,b,t}$, where U_{tank} the tank conductivity. Finally, (18) dictates that for every building b, the DHW tank temperature must reach the desired temperature T_{dhw}^{des} at the desired time t_{dhw}, which has been set at 09:00 for commercial buildings, and 07:00 or 19:00 for residential buildings (see Table 3).

$$T_{sp}^{n,b,t} = T_{sp_{init}}^{n,b} + \Delta t \sum_{t_{st}}^{t} \frac{Q_{tot_{sp}}^{n,b,t}}{C_b + V_b C_{air} \rho_{air}} \tag{19}$$

$$Q_{tot_{sp}}^{n,b,t} = Q_{hp_{sp}}^{n,b,t} m^{n,b} + Q_{irr}^{n,b,t} - Q_{los_{sp}}^{n,b,t} \tag{20}$$

$$Q_{los_{sp}}^{n,b,t} = (\sum_{sf} U_{sf} A_{sf} + C_{air}\, \rho_{air}\, r_b)(T_{sp}^{n,b,t} - T_a^t) \tag{21}$$

The building temperature dynamics $T_{sp}^{n,b,t}$ are modeled in (19), which depend on the initial building temperature $T_{sb_{init}}^{n,b}$ and the total space heating gains and losses $Q_{tot_{sp}}$ divided by the thermal capacity of the building mass C_b and the capacity of the building air where V_b, C_{air}, and ρ_{air} the building volume, the air-specific capacity and air density, respectively. Equation (20) denotes that $Q_{tot_{sp}}$ comprise the HP heating output $Q_{hp_{sp}}$, the heating gains from irradiation Q_{irr}, and the total heating losses $Q_{los_{sp}}$ where m denotes the HP mode (+1/-1 for heating/cooling). The total heating losses $Q_{los_{sp}}$ depend on the conduction losses (first term) and ventilation losses (second term), which depend highly on the ambient temperature T_a as shown in (21). The former also depends on the sum of the conductivity U over the area A of every building surface, while the latter also depends on the building air change rate r_b.

$$P_{hp_{dhw}}^{n,b,t} \leq b_{sp} P_{hp_{dhw}^{max}}^{n,b} \tag{22}$$

$$P_{hp_{sp}}^{n,b,t} \leq b_{sp} P_{hp_{sp}^{max}}^{n,b} \tag{23}$$

$$b_{sp} + b_{dhw} \leq 1 \tag{24}$$

$$P_{hp_{tot}}^{n,b,t} = P_{hp_{sp}}^{n,b,t} + P_{hp_{dhw}}^{n,b,t} \tag{25}$$

In (22)–(24), the binary variables b_{sp}, b_{dhw} are introduced to enforce that the HP power consumption for DHW $P_{hp_{dhw}}^{n,b,t}$ and for space heating/cooling $P_{hp_{sp}}^{n,b,t}$ cannot occur simultaneously, where $P_{hp_{dhw}^{max}}^{n,b}$ and $P_{hp_{sp}^{max}}^{n,b}$ the respective maximum power limits. Additionally, (25) dictates that the total HP power consumption $P_{hp_{tot}}^{n,b,t}$ is always the consumption for the space heating/cooling and DHW.

$$\begin{aligned} c_{p_{hp}}^{n,b,t} &= 7.90471e^{-0.024(T_{ret}^{n,b,t} - T_a^t)} = 7.90471e^{c_{exp}^{n,b,t}} : \\ c_{exp}^{n,b,t} &= -0.024(T_{ret}^{n,b,t} - T_a^t) \end{aligned} \tag{26}$$

$$T_{ret}^{n,b,t} = T_{sup}^{sp/dhw} - Q_{hp_{sp/dhw}}^{n,b,t} / (\dot{m}_{wat} C_{wat}) \tag{27}$$

Equation (26) dictates the original model of the HP's coefficient of performance (COP) as derived by [47], which depends on the ambient temperature and the dynamic HP's return water temperature $T_{ret}^{n,b,t}$. Due to the non-linearity of (26), the exponential part is defined as $c_{exp}^{n,b,t}$, and a piecewise linear approximation has been utilized for the COP modeling. Moreover, the HP's return water temperature is modeled in (27), where $\dot{m}_{wat}$: the flow water rate and T_{sup} the supply water temperature, which is set at 35°, 50°, and 18° for floor-heating, DHW, and floor-cooling, respectively.

$$\begin{aligned} Q_{hp_{sp/dhw}}^{n,b,t} &= P_{hp_{sp/dhw}}^{n,b,t} c_{p_{hp}}^{n,b,t} : \\ 0 \leq Q_{hp_{sp/dhw}}^{n,b,t} &\leq Q_{hp_{sp/dhw}^{max}}^{n,b} \end{aligned} \tag{28}$$

$$P_{pv_{dev}}^{n,b,t} = P_{pv_{max}}^{n,b,t} - P_{pv_{use}}^{n,b,t} : 0 \leq P_{pv_{use}}^{n,b,t} \leq P_{pv_{max}}^{n,b,t} \tag{29}$$

$$T_{dev}^{n,b,t} = \max(T_{sp}^{n,b,t} - T_{high}^{n,b}, T_{low}^{n,b} - T_{sp}^{n,b,t}, 0) : T_{min}^{n,b} \leq T^{n,b,t} \leq T_{max}^{n,b} \tag{30}$$

Consequently, (28) dictates the relation between the HP power consumption for space heating/cooling and DHW with the COP and their respective heating output amounts limited to the HP heating capacity $Q_{hp_{sp/dhw}^{max}}^{n,b}$. These equations are the only non-linear equations of the power control model that make the problem MIQP. The instantaneous PV curtailment amount $P_{pv_{dev}}$ is dictated in (29) where $P_{pv_{max}}$ & $P_{pv_{use}}$ the PV generation and used PV power, respectively. The temperature deviation

Preprints.org (www.preprints.org) | NOT PEER-REVIEWED | Posted: 16 June 2026 doi:10.20944/preprints202606.1277.v1

T_{dev} is defined in (30) as the temperature difference from the nearest desired temperature interval limit $T^{n,b}_{low}$ or $T^{n,b}_{high}$. The desired temperature interval $[T^{n,b}_{low}, T^{n,b}_{high}]$ has been set at [21°, 23°], while for the needs of the model, the maximum temperature interval $[T^{n,b}_{min}, T^{n,b}_{max}]$ has been set at [17°, 27°]. The variables $P_{pv_{dev}}$ and T_{dev} are used in the objective function with cost penalties (such as with EV charging) to ensure PV max self-consumption and thermal comfort, respectively. The big-M method has been used for the linearization and integration of (30) in the PCS model, for which the reader is referred to [45]. Figure 2 depicts an intuitive explanation of (30), while Table 3 summarizes the parameters of this section.

Table 3. Building Parameters of Coordinated Power Control Model.

Par.	Explanation	Value
$C^{n,b}_{hp_{pen}}$	Discomfort Penalty	10€/(°C Δt)
$C^{n,b}_{pv_{pen}}$	PV Curtail. Penalty	10€/(kW Δt)
C_b	Build. Thermal Capacity	$4.755kWh/K$
V_b	Build. Volume	$585m^3$
C_{air}	Air Thermal Capacity	$0.279Wh/kgK$
ρ_{air}	Air Density	$1.225kg/m^3$
C_{wat}	Water Thermal Capacity	$1.16kWh/kgK$
ρ_{wat}	Water Density	$993kg/m^3$
r_b	Air Change Rate	$0.3h^{-1}$
$T^{n,b}_{min}$	Build. Min Temp.	17°
$T^{n,b}_{max}$	Build. Max Temp.	27°
$T^{n,b}_{high}$	High Comfort Temp.	23°
$T^{n,b}_{low}$	Low Comfort Temp.	21°
$M1, M2$	Big-M Parameters	10
T_{sup}	HP Supply Temp.: space heating, cooling & dhw	35°, 18°& 50°
$T^{n,b}_{sp/dhw_{init}}$	Initial space/DHW Temp.	22°
T^{des}_{dhw}	Desired DHW Temp.	50°
N_p	People per build.	4
R_{tank}, H_{tank}	Tank Radius & Height	0.23m & 1.3m
V_{tank}	Tank Volume	215l
U_{tank}	Tank Conductivity	$5.98W/Km^2$
$\dot{m}_{wat}$	HP water flow rate	$0.8kg/s$
V_{w_p}	Water Volume/person	$65l$

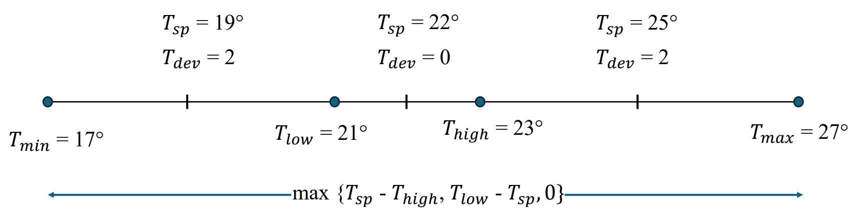

Figure 2. Intuitive explanation of T_{dev} by (30).

Preprints.org (www.preprints.org) | NOT PEER-REVIEWED | Posted: 16 June 2026 doi:10.20944/preprints202606.1277.v1

4.3. Node Constraints

The node constraints below constitute the node power balance, and the grid input and output power limits. All the node constraints apply for $\forall t \in T$.

$$P_{im}^{n,t} - P_{ex}^{n,t} = \sum_{j=1}^{J} \left(\frac{P_{ch}^{n,j,t}}{h_{ch}^{n,j}} - P_{dis}^{n,j,t} h_{ch}^{n,j} \right) + \frac{P_{ch}^{n,bes,t}}{h_{bes}^{n}} - P_{dis}^{n,bes,t} h_{bes}^{n} + \sum_{b=1}^{B} \left(P_{hp_{tot}}^{n,b,t} + P_{l}^{n,b,t} - P_{pv}^{n,b,t} \right) \tag{31}$$

The power balance is dictated in (31), which defines that the difference between the dynamic node imported $P_{im}^{n,t}$ and exported $P_{ex}^{n,t}$ power is the total EV/BESS charging power, HP power consumption, and base load demand cover minus the total PV rooftop generation and EV/BESS discharging power. The parameters $h_{ch}^{n,j}, h_{bes}^{n}$ constitute the EV charger and BESS efficiencies, set at 0.95 and 0.98 respectively. The EV charger efficiency also comprises the EV battery losses and the BESS efficiency, and the power converter losses. The losses due to power conversion for BESS operation are lower than the respective of EV (dis)charging due to the lower needed conversion stages; power conversion for EV (dis)charging needs an additional isolation stage. Finally, (32) and (33) dictate that all the node composite power is always lower than the input and output node capacity limits, G_{in}^{n} and G_{out}^{n}, respectively, and force the node not to import and export power simultaneously.

$$P_{im}^{n,t} = \sum_{j=1}^{J} \left(\frac{P_{ch}^{n,j,t}}{h_{ch}^{n,j}} - P_{dis}^{n,j,t} h_{ch}^{n,j} \right) + \frac{P_{ch}^{n,bes,t}}{h_{bes}^{n}} - P_{dis}^{n,bes,t} h_{bes}^{n} + \sum_{b=1}^{B} \left(P_{hp_{tot}}^{n,b,t} + P_{l}^{n,b,t} - P_{pv}^{n,b,t} \right) \leq G_{in}^{n} \tag{32}$$

$$P_{ex}^{n,t} = \sum_{b=1}^{B} \left(P_{pv}^{n,b,t} - P_{hp_{tot}}^{n,b,t} - P_{l}^{n,b,t} \right) + P_{dis}^{n,bes,t} h_{bes}^{n} - \frac{P_{ch}^{n,bes,t}}{h_{bes}^{n}} - \sum_{j=1}^{J} \left(\frac{P_{ch}^{n,j,t}}{h_{ch}^{n,j}} - P_{dis}^{n,j,t} h_{ch}^{n,j} \right) \leq G_{out}^{n} \tag{33}$$

4.4. Battery Degradation

Since the PCS performs energy arbitrage by using V2G and a higher number of equivalent cycles of the BESS to take advantage of the daily price deviations, it is important that the additional battery degradation cost is considered during PCS power scheduling.

4.4.1. Non-Linear Model

$$Q_{cal} = k_{cal} e^{-\frac{E_a^C}{R}\left(\frac{1}{T} - \frac{1}{T^r}\right)} e^{\frac{\alpha F}{R} \frac{U_a^r - U_a}{T^r}} + k_0) \sqrt{t} \tag{34}$$

$$Q_{cy,1} = k_{cy,1} e^{-\frac{E_{a,cy1}}{R}\left(\frac{1}{T} - \frac{1}{T^r}\right)} \sqrt{q_{tot}} \tag{35}$$

$$Q_{cy,2} = k_{cy,2} e^{-\frac{E_{a,cy2}}{R}\left(\frac{1}{T} - \frac{1}{T^r}\right)} e^{\beta \frac{I_{ch} - I_{ch}^r}{c}} \sqrt{q_{ch}} \tag{36}$$

The original battery degradation model dictated by (34)–(36) has been developed in [48] for an LFP cell, designed for stationary applications. More specifically, (34) models the calendar battery aging that depends mainly on the operating temperature T, SOC via the anode potential U_a, and time t, where T^r the rated temperature (25°) and U_a^r the anode potential at the rated SOC ($SOC^r = 50\%$). The cyclic aging is dictated by (35)–(36), where $I_{ch/dis}^{r,cell}$ the rated cell charging and discharging current; two equations are used for cyclic aging because different aging mechanisms are energized during charging and discharging. More in particular, (35) depends on temperature and total throughput q_{tot}; thus, it is activated during both charging and discharging. On the contrary, (36) depends on temperature, charging throughput q_{ch}, and current I_{ch}; thus, it is activated only during charging. All variables in (34)–(36) refer to the battery cell, while Table 4 summarizes the degradation parameters.

4.4.2. Model Linearization

The original model cannot be integrated into the MIQP problem as is because it is highly non-linear and comprises multiplication of many exponential and square-root terms. Therefore, it has been linearized by transforming it to its equivalent in the logarithmic scale.

$$\bar{Q}_{cal}(25^{\circ}, SOC = 50\%) = k_{cal}(1 + k_0)\sqrt{t = 1day} \tag{37}$$

$$ln(Q_{cy,1}) = ln(k_{cy,1}) + 0.5ln(q^{cell}_{tot}) \tag{38}$$

$$ln(Q_{cy,2}) = (ln(k_{cy,2}) - \frac{\beta I^{r,cell}_{ch}}{c}) + \frac{\beta}{c} I^{cell}_{ch} + 0.5ln(q^{cell}_{ch}) \tag{39}$$

Equations (37)–(39) represent the linearization of the degradation model (34)–(36). Concerning the calendar aging and (34), the duration of the simulation is fixed at one day, the BESS SOC is maintained at 50% at the beginning and end of the day, and a thermal management system is assumed to keep the operation temperature at 25°. Hence, a mean calendar capacity loss is used for the day, and (34) is transformed to (37). Moreover, assuming again a maintained temperature at 25°and using the logarithmic properties, (35) and (36) are transformed to their equivalents in the logarithmic scale (38) and (39), respectively.

4.4.3. Integration into the MIQP Model

Equation (40) correlates the EV and BESS charging and discharging currents with the cell charging and discharging currents of the respective assets $I^{n,cell-j/bes,t}_{ch}$ and $I^{n,cell-j/bes,t}_{dis}$, which are rated at $I^{r,cell}_{ch/dis} = 3A$ [48]. Furthermore, the total cell current $I^{n,cell-j/bes,t}_{tot}$ is dictated in (41).

$$I^{n,cell-j/bes,t}_{ch/dis} = (I^{n,j/bes,t}_{ch/dis} / I^{n,j/bes}_{max}) I^{r,cell}_{ch/dis} \quad \forall t \in T \tag{40}$$

$$I^{n,cell-j/bes,t}_{tot} = I^{n,cell-j/bes,t}_{ch} + I^{n,cell-j/bes,t}_{dis} \quad \forall t \in T \tag{41}$$

Moreover, (42) models the EV and BESS total and charging cell throughput dynamics $q^{n,cell-j/bes,t}_{tot,ch}$, which are needed for the calculation of $ln(q_{tot,ch})^{cell-j/bes}$ in (38) and (39) with the use of the parameter $\lambda = 10^{-7}$ to avoid infinity at zero current. Additionally, (43) dictates the limits of the cell total and charging current, and throughput.

$$q^{n,cell-j/bes,t}_{ch/tot} = I^{n,cell-j/bes,t}_{ch/tot} \Delta t + \lambda \quad \forall t \in T \tag{42}$$

$$\begin{aligned} 0 \leq I^{n,cell-j/bes,t}_{ch}, I^{n,cell-j/bes,t}_{tot} &\leq 3 \quad \forall n,\ t \in T \\ 0 \leq q^{n,cell-j/bes,t}_{ch}, q^{n,cell-j/bes,t}_{tot} &= 3\Delta t \quad \forall n,\ t \in T \end{aligned} \tag{43}$$

The variables q_{ch} and q_{tot} are transformed to their equivalent $ln(q_{ch})$ and $ln(q_{tot})$, respectively, using linear piecewise approximations of the function $y = ln(x)$, while $ln(Q_{cy,1})$ and $ln(Q_{cy,2})$ are similarly transformed to their equivalent $Q_{cy,1}$ and $Q_{cy,2}$, using the function $x = e^y$. The resulting degradation variables Q_{cal}, $Q_{cy,1}$ and $Q_{cy,2}$ constitute capacity loss percentages. In this regard, (44) represents the degradation objective, which minimizes the total BESS/EV cyclic aging with the addition of the mean BESS/EVs' calendar aging $\bar{Q}_{cal}$. Finally, the total BESS/EV battery aging is calculated post-optimization with the original model (34)–(36) for verification purposes.

 doi:10.20944/preprints202606.1277.v1

$$
\begin{aligned}
\min B_{Qtot}^{n} = \min \Delta t(\sum_{t=1}^{T}(Q_{cy,1}^{n,bes,t} + Q_{cy,2}^{n,bes,t})B_r^{n,bes} + \\
\sum_{j=1}^{J}(Q_{cy,1}^{n,j,t} + Q_{cy,2}^{n,j,t})B_r^{n,j}) + Q_{cal}^{\bar{n},bes}B_r^{n,bes} + \sum_{j=1}^{J} Q_{cal}^{\bar{n},j}B_r^{n,j}
\end{aligned}
\tag{44}
$$

The utilized empirical degradation model considers various degradation factors such as temperature, time, C-rate, and throughput. However, it fails to consider the effects of SOC and depth of discharge (DOD), especially for the cyclic aging. Therefore, there is an accuracy loss for cycling during very high SOCs, and DODs.Therefore, the following measures have been considered:

1) Stationary BESS: The SOC is directly limited to deviate within the interval [10%, 90%] so that the battery is never completely depleted or charged.

2) EVs: Firstly, the EVs are allowed to participate in the power control only after their SOC reaches 20%. Secondly, due to the CC-CV region, the EVs actively perform energy arbitrage when they are being charged in the CC region. When $SOC > 90\%$, the EVs stop being consecutively charged and discharged due to the low power levels, and afterwards are charged uncontrollably until departure.

4.5. Objective Function

Finally, the power control objective function for every node n is dictated in (45). The PCS is a multi-objective MIQP model that has translated all objectives into a total cost aimed to be minimized. In this regard, all penalty costs are chosen to be much higher than the energy price to attach great importance to the customers' comfort (see Tables 2 and 3). The total cost comprises:

a) For energy arbitrage: The minimum exchange grid power cost where P_{im}, C_{buy} and P_{ex}, C_{sell} the imported and exported power and related costs.

b) For PV max self-consumption: The total PV curtailment cost, where $C_{pv_{pen}}$ the related penalty.

c) For thermal comfort maintenance: The total thermal discomfort cost, where $C_{hp_{pen}}$ the related penalty and $O^{t,n,b} \in [0, 1]$ the dynamic building occupancy.

d) For charging comfort maintenance: The total EV unfinished charging cost, where $C_{pv_{pen}}$ the related penalty.

e) For battery degradation mitigation: The total battery degradation cost, where C_Q^n the degradation cost of 150€/kWh [49]. The placement of (44) inside (45) directly mitigates battery degradation. In this work, the weights of the different objectives have been adjusted in association with the respective costs. However, placing a higher weight would give a higher importance to battery degradation minimization and hence, directly decrease it through the objective function.

All power control parameters used in Section 4 for the modeling of EV/BESS, buildings, and battery degradation are summarized in Tables 2, 3, and 4, respectively. Overall, the main modeling novelty is the development and testing of the linearized physics-guided semi-empirical highly non-linear battery degradation model. Moreover, the developed multi-objective function and the simultaneous optimization of all the objectives (EV charging, thermal comfort maintenance, PV max self-consumption, energy arbitrage, battery degradation minimization) are the second main novelty.

$$
\min C_n = \Delta t(\sum_{t=1}^{T}(P_{im}^{n,t}C_{buy}^{t} - P_{ex}^{n,t}C_{sell}^{t})) + \sum_{t=1}^{T}\sum_{b=1}^{B}(P_{pv_{dev}}^{n,b,t}C_{pv_{pen}}^{n,b}) + \sum_{t=1}^{T}\sum_{b=1}^{B}(T_{dev}^{n,b,t}C_{hp_{pen}}^{n,b}O^{t,n,b}) + \sum_{j=1}^{J}E_g^{n,j}C_{ev_{pen}}^{n,j} + B_{Qtot}^{n}C_Q^n \tag{45}
$$

doi:10.20944/preprints202606.1277.v1

Table 4. Battery Degradation Parameters of Coordinated Power Control Model.

Par.	Explanation	Value
k_{cal}	Calendar coefficient in (37)	$3.694 * 10^{-4}$
k_0	Constant in (37)	0.142
$k_{cy,1}$	Cyclic coefficient in (38)	$1.456 * 10^{-4} Ah^{-0.5}$
$k_{cy,2}$	Cyclic coefficient in (39)	$4.009 * 10^{-4} Ah^{-0.5}$
β	Constant in (39)	2.64h
C	Cell capacity	3Ah
$I_{ch}^{r,cell}$	Rated Cell Current	3A
C_Q^n	Degradation Cost	$150€/kWh$
λ	Constant in (42)	10^{-7}

5. Case Studies & Scenarios

5.1. Small (3-Node) & Large (13-Node) LV Grids

Two grid scenarios have been used for the testing of the PCS. The small grid scenario consists of 3 nodes from different areas (residential, commercial, and mixed). It has been assumed that the three nodes are connected with different radial feeders to the main grid. Each node comprises a 50kWh-rated BESS unit of 0.5C max C-rate, while Figure 3 (a) depicts the number of buildings and chargers per node. Buildings in residential areas, e.g. households (HHs), are occupied longer during the day (00:00-08:00, 14:00-00:00) compared to commercial buildings such as offices and stores that are mostly occupied during the day (09:00-21:00). Moreover, home chargers at residential areas are characterized by a lower frequency of incoming EV fleets which remain parked for longer times and arrive with lower SOCs compared to public and semi-public chargers. Furthermore, EVs consume approximately a 30% higher amount of energy due to cabin heating [4] during Winter, while building heating consumes 50% higher amount of energy than building cooling during Summer because of a higher temperature difference with ambient temperature (hence, lower COPs) [46]. Finally, the input and output node capacity limits, G_{in}^n and G_{out}^n respectively, are set at 400kW.

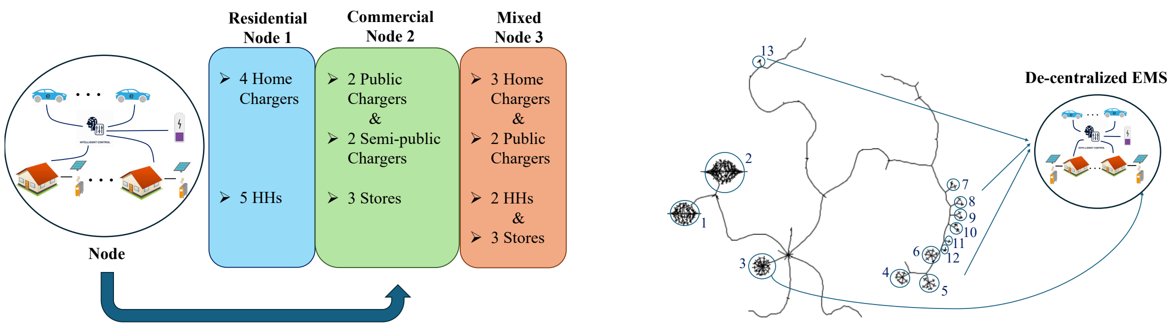

(a) (b)

Figure 3. Description of the two DG scenarios: (**a**)Node concept & characteristics in small grid scenario. (**b**) Distributional EMS of the large grid scenario with the use of aggregators.

The large grid scenario is depicted in Figure 3 (b) and is a real urban grid in the Netherlands. Each one of the 13 load locations, hereby called nodes, comprises several loads (buildings) equipped with PVs, HPs, and EV chargers. Table 5 summarizes the number of LCTs at every node. Moreover, a BESS is installed at every node, whose capacity is set at 10kWh per building/charger. Finally, the input and output node capacity limits, G_{in}^n and G_{out}^n respectively, are set at 3.785MW for the large grid example.

Table 5. Node Characteristics of Large Grid Scenario.

Nodes	Buildings (PVs, HPs)	Chargers	BESS Capacity [kWh]
1	32	32	320
2	44	44	440
3	18	18	180
4	6	6	60
5	6	6	60
6	6	6	60
7	2	2	20
8	2	2	20
9	2	2	20
10	2	2	20
11	1	1	10
12	1	1	10
13	1	1	10

5.2. Data Input

The following data are used as input in the power control:

(1) Dutch residential and commercial electricity distribution consumption profiles have been acquired from [50].

(2) Probability distribution functions (PDFs) of EV driving patterns, such as arrival and departure times, arrival SOCs, and requested energy by the Elaad open database [2].

(3) Weather data, such as ambient temperature, incident irradiation, wind speed, etc., which have been used for the creation of the PV generation profiles and the heating losses calculation, by the Meteonorm database [51].

(4) Day-ahead market (DAM) energy price profiles have been acquired by the Dutch ENTSO-E platform [52].

(5) The LV distribution grid used in the large grid scenario was acquired by the Dutch distribution system operator (DSO) Enexis Groep [3].

(6) A 3kW-rated Dimplex LIK 8MER reversible HP module and a 3kW-rated HIT N245 PV module for the building heating and PV generation, respectively. Moreover, the EV pool comprises the 11kW-rated "Hyundai Kona, BMW I3, Jaguar I-Pace, and Tesla Model 3", the 16kW-rated "Tesla Model X and Tesla Model S", and the 22kW-rated "Renault Zoe" EVs.

(7) The Sony US26650FTC1 LIB iron phosphate/graphite cell of 3.2V and 3Ah nominal voltage and capacity, designed for stationary applications, derived by [48].

To incorporate a level of uncertainty, Monte-Carlo Simulation has been used to generate a) 600 random EV fleet profiles for Home, Semi-public, and Public chargers from the PDFs of (2), b) 200 residential and commercial building occupancy profiles with random occupancy changes, as discussed in Section 3, and c) 180 Summer and Winter PV generation profiles with random PV module orientations using the data of (3) and PV modeling in [46]. Afterwards, LCT profiles have been randomly selected and distributed in the utilized grid scenarios.

5.3. Overall Case Studies

Table 6 summarizes the case studies of this work with their respective simulation times. Cases 1-6 are devoted to the small grid scenario, and Cases 7-12 to the large grid scenario. Cases 1, 3, and 5 investigate the power control of flexible loads, flexible loads + BESS, and flexible loads + BESS + degradation for Winter, while Cases 2, 4, and 6 investigate the related comparisons during Summer. Accordingly, the same applies to the large grid scenario in Cases 7-12. Overall, the case studies

[2] https://platform.elaad.io
[3] https://www.enexisgroep.com/

described above aim to quantify and reflect on the effect of the following influencing factors on power control characteristics (control cost, grid power exchange amount, V2G energy use, BESS energy use, power flows scheduling, etc):

Table 6. Case Studies and Scenarios of Power Control.

Cases	Flexibility	Season	Scenario	Degr.	Time
1	Loads	Winter	Small Grid	No	38′
2	Loads	Summer	Small Grid	No	37′
3	Loads & BESS	Winter	Small Grid	No	41′
4	Loads & BESS	Summer	Small Grid	No	41′
5	Loads & BESS	Winter	Small Grid	Yes	1h & 2′
6	Loads & BESS	Summer	Small Grid	Yes	59′
7	Loads	Winter	Large Grid	No	7h & 50′
8	Loads	Summer	Large Grid	No	7h & 45′
9	Loads & BESS	Winter	Large Grid	No	8h & 5′
10	Loads & BESS	Summer	Large Grid	No	7h & 55′
11	Loads & BESS	Winter	Large Grid	Yes	10h & 3′
12	Loads & BESS	Summer	Large Grid	Yes	9h & 57′

1) Flexibility of loads and BESS: Stationary BESS and flexible loads, such as EVs and HPs, can both offer flexibility for energy arbitrage. While the BESS is expected to be capable of the highest flexibility because it is not prone to uncertainties, the contribution of flexible loads can be proven comparable in large grids.

2) Grid-size and grid-type effect: Different grid types, such as residential and commercial, can highly influence the power control decision-making due to different characteristics of buildings and EV fleets. Additionally, a larger grid that comprises a higher number of present flexible loads can be proven to be more flexible, also without the use of a BESS.

3) Seasonal effect: Different seasons can have a significant impact on the consumption and power levels of the flexible loads as well as on the PV generation. Thus, it is important to encapsulate the yearly seasonal variations in the investigation of the power control performance.

4) Battery degradation effect: Constant battery charging and discharging can highly increase the steepness of the capacity fading and induce further costs. Therefore, especially in large grids, accumulated degradation costs can become significant and alter the energy arbitrage decision-making.

5.4. Simulation Setup & Utilized Software

The simulation timestep has been set to 5 minutes to show in detail the power flow decision-making of the PCS with a reasonable computational time. Moreover, the simulation duration was set to 1 day for both Winter and Summer seasons. Concerning the utilized software, the model was developed in a Python 3.9 environment and was solved with Gurobi 11 solver due to its powerful capabilities in solving MIP problems. Finally, the simulations were performed with an Intel (R) 11th Gen Core(TM) i7-3.00GHz processor with 16GB installed RAM.

5.5. Limitations

The main limitations of this work are: Firstly, the uncertainties considered are the building occupation and the EV driving patterns. However, there are multiple other uncertainties in PCS, such as PV generation, load demand, etc., which should also be managed on Level 2 using the re-optimization of RHO. Secondly, daily simulations were performed due to computational time. The selection of a weekly simulation, which would be the closest to the average of the season, would provide more insights, such as intra-week effects. Thirdly, modeling non-linearities (e.g., CC-CV, COPs) has been integrated with piecewise linear functions in the MIQP problem, while charging efficiencies, which are power-dependent, have been considered steady. Their consideration with the use of a non-linear solver is proposed for future work to address the level of accuracy decrease. Moreover, while the empirical battery degradation model accounts for most degradation mechanisms (time, C-rate, temperature, throughput, etc.), it does not consider the effects of high SOC and DOD on cyclic aging. Finally, all loads at each location of the large grid are aggregated and optimized together as a node, neglecting the effect of the distribution lines between them due to their much shorter length compared to the other lines of the grid. The consideration of the power losses on these lines is also proposed for future work.

6. Results

The results of the two grid scenarios for Level 1 are presented below. Apart from some numerical differences due to the forecast error corrections, the insights of the work remain similar for Level 2.

6.1. Small Grid Scenario

6.1.1. Power Control without BESS

The power flows of Node 3 for Winter Cases 1,3, 5, and Summer Cases 2, 4 are depicted with the daily energy prices in Figures 4(a) and (b), respectively. In Case 1 (Figure 4(a)), grid power is imported during low energy prices [00:00-07:00] for building and DHW heating, while during [07:00- 09:00], power is imported only for base load cover. Moreover, the highest energy price peak during [17:00-19:00] is avoided, and EVs are charged during the periods [16:00-17:00] and [19:00-00:00]. Additionally, V2G energy is utilized during the highest price peak to cover the base load demand. Finally, PV generation covers the load and is mostly exported because it coincides with the high energy prices [09:00-16:00]. On the contrary, in Case 2 (Figure 4(b)), the higher and prolonged Summer PV generation is initially exported during the increasing energy prices of [05:00-10:00] and is consequently used until 19:00 for EV charging, load cover, building cooling, etc. Similarly, the high energy price peak of [19:00-20:00] is mostly avoided, while V2G energy is not preferred due to the availability of PV generation, which causes lower power losses.

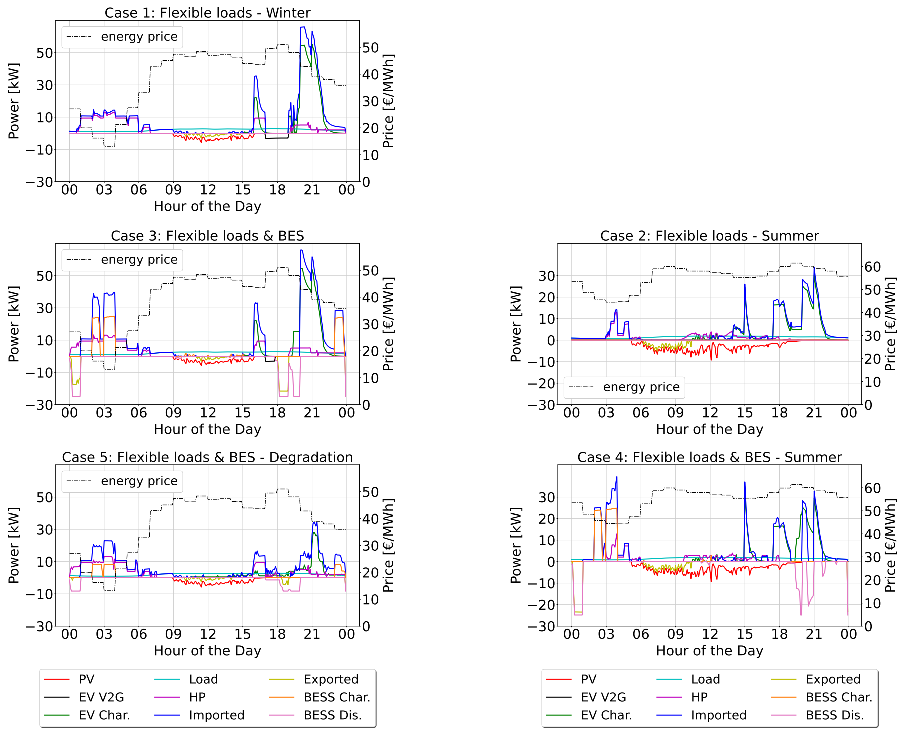

(a) (b)

Figure 4. Small grid scenario: (**a**) Power Flow of Node 3 for Winter Cases 1, 3 & 5. (**b**)Power Flow of Node 3 with and without BESS for Summer (Cases 2 & 4).

6.1.2. Power Control with BESS

In Figure 4(a), PV generation use, EV charging, and HP operation remain similar for Cases 1 and 3. BESS is mostly charged with grid power during the lowest energy prices of [02:00-04:00], is discharged back to the grid during the highest prices of [18:00-19:00], while it is also used for EV charging and base load cover during [19:00-20:00]. Additionally, the V2G energy use during the high energy prices is considerably decreased compared to Case 1, and BESS use is preferred due to the lower power losses. Similarly, in Cases 2, 4 of Figure 4(b), the control of PV generation and flexible loads behaves the same as in Cases 1 and 3. However, while BESS is mainly charged again during the low prices of [02:00, 04:00], it is discharged for EV charging during the high energy prices of [19:00, 21:00]. Hence, BESS is used more for the flexibility of the node in Case 4, because most revenues are ensured by the PV generation. On the contrary, BESS is used in Case 3 mostly for revenues and cost compensation to compensate for the high imported grid energy due to the low PV availability.

6.1.3. Power Control with Battery Degradation

Regarding Case 5 in Figure 4(a), the BESS charging and discharging periods remain similar with and without consideration of battery degradation cost; however, the power levels are notably decreased. Moreover, the discharged BESS energy is more utilized for building heating and EV charging than for power exportation to the grid for revenues. Hence, the BESS use is highly decreased and is preferred only for the basic needs of the node (EV charging and building heating without penalty costs) during the high energy price peaks of [17:00, 20:00]. Additionally, V2G energy is not used due to the combined high round-trip power losses and additional degradation costs. Finally, Table 7 summarizes the daily capacity fading in (Wh) and the yearly extrapolation in (%) for the BESS for all nodes and Cases 3-6, showing the effectiveness of the degradation optimization model. For example, while BESS capacity fading is approximately 2.5% in Case 3, it drops to 1.8% in Case 5.

Table 7. BESS Capacity Fading for Nodes 1-3: Cases 3-5 & Cases 4-6.

	Case 3		Case 5		Case 4		Case 6	
Nodes	Daily (Wh)	Yearly (%)	Daily (Wh)	Yearly (%)	Daily (Wh)	Yearly (%)	Daily (Wh)	Yearly (%)
Node 1	3.49	2.54	2.35	1.72	2.88	2.1	1.71	1.24
Node 2	3.66	2.68	2.47	1.8	2.72	1.98	1.34	0.98
Node 3	3.41	2.48	2.4	1.76	2.29	1.76	1.16	0.84

6.1.4. Power Control Cost & Grid Power Exchange Summary

Figure 5(a) depicts in the upper plot the total imported and exported energy and in the lower plot the total cost (energy cost and degradation cost) of the 3 nodes. Winter cases 1, 3, and 5 have always had higher costs than their respective Summer cases 2, 4, and 6 (up to 60%) because of the higher amount of imported power, as discussed in Section 5. For example, Node 1 imported 240kWh and 110kWh in Cases 1 and 2, respectively, (118% increase). Moreover, using a higher PV generation in Summer reduces the total cost, either with direct use or with grid exportation for revenues. Overall, Cases 1-2 export the least amount of energy for all nodes, since they are the least flexible (no BESS). Furthermore, BESS use addition decreases the cost for most nodes by a factor up to 16% (Node 3 in Case 3 compared to Case 1), while the amounts of imported and exported grid power are also increased for all nodes when Cases 3 and 4 are compared to Cases 1 and 2, respectively. Additionally, in battery degradation Cases 5 and 6, the total cost always increases for all nodes when comparing them with their respective Cases 3 and 4. While the energy cost can be lower (e.g., Node 1 in Case 5 compared to Case 3) due to lower grid power exchange to avoid higher degradation, when the degradation cost is summed up, the total cost results are always equal to or higher.

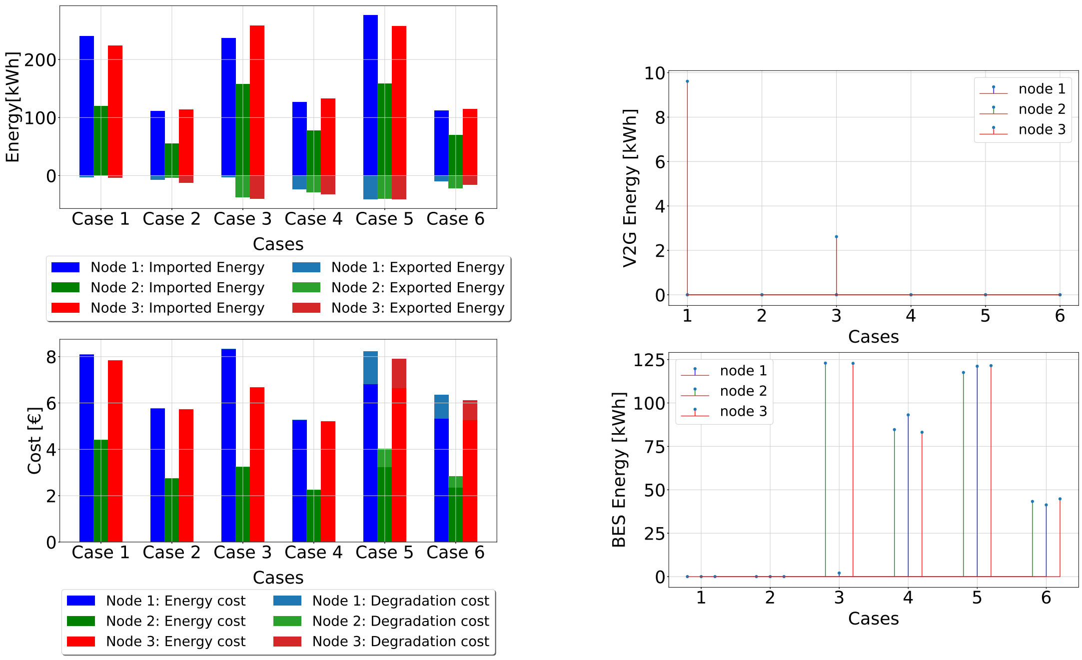

(**a**) (**b**)

Figure 5. Small grid scenario analysis: (**a**) Daily Energy and Degradation Cost (lower plot) and Grid Power Exchange (upper plot) for Nodes 1-3 and Cases 1-6. (**b**)BESS energy use (lower plot) and V2G energy use (upper plot) for Nodes 1-3 and Cases 1-6.

The node type also strongly impacts the exchanged grid power and total cost. The commercial node (Node 2) is generally characterized by a lower cost in all cases. This is because, as explained, commercial buildings (e.g., stores and offices) are occupied less during the day than residential buildings, and EVs are parked for a lower parking time in public chargers and request a lower amount of energy. Hence, the needed imported grid power is considerably lower (by approximately 50%) for the commercial node. For that reason, there is also more power window in the feeder to export BESS energy and PV generation for revenues, and hence, Node 2 exports considerably more power when BESS is introduced; almost comparable to Node 3, which is the most flexible node. Hence, highly flexible nodes or nodes that occupy less of the power capacity can use their BESS capacity more for revenues. Finally, the degradation cost is always higher for Nodes 1 and 3 because they comprise home chargers where EVs arrive with a lower SOC and request higher amounts of energy.

6.1.5. BESS Energy & V2G Energy Use Summary

Regarding the use of BESS and V2G, Figure 5(b) depicts the total V2G energy used (upper plot) and the total BESS energy used (lower plot) per node and case. V2G is used only in Winter Cases 1 and 3, because PV generation is available for a shorter time. For example, V2G energy is generally used during high energy price peaks. During the Winter price peaks of [17:00-20:00], there is no more available PV generation. Moreover, concerning all other cases, BESS use is always preferred over V2G due to the higher BESS efficiency and lower power losses. The influence of seasonal variations of PV generation on V2G energy use has also been seen in [45]. In Cases 5 and 6, where there is additional degradation cost combined with the power losses, V2G energy use becomes inefficient even during Winter. Finally, V2G energy is more likely to be used in Node 3 (the mixed node), which has the highest flexibility, comprising both residential and commercial buildings, and home and (semi-)public chargers. Regarding BESS energy use, as already discussed, Winter (Cases 3 and 5) favors using BESS for charging and discharging power to the grid for revenues for most of the nodes. On the contrary, the available PV generation is preferred during Summer for power exportation, and the BESS is mostly

 doi:10.20944/preprints202606.1277.v1

used for the needs of the node instead. Finally, the consideration of battery degradation decreases the use of BESS, especially during Summer, due to the additional degradation cost.

6.2. Large Grid Scenario

6.2.1. Flexible Loads and BESS

Figure 6 shows in plots (a) and (b) the power flows of Nodes 2 and 6, respectively, of the large grid scenario for Case 9 (BESS use during Winter). Some of the previous observations from the small grid scenario can also be seen here. For example, most building heating and EV charging are performed during the low energy price periods; hence, in the morning before 08:00 and in the evening after 19:00. However, in contrast with the small grid, less PV generation is exported to the main grid for revenues during Winter, while a considerable amount is used for building heating and EV charging. Hence, in large grids, which comprise many loads (buildings and chargers), PV self-consumption is increased, and grid power exportation is decreased. This is because when a high number of loads are constantly present at a grid, more power is consistently needed during the day, and hence, available PV power will be firstly utilized to cover their consumption.

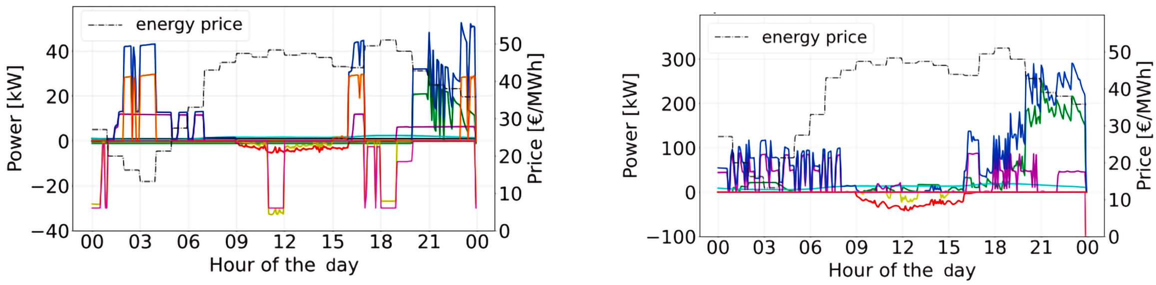

(**a**) (**b**)

Figure 6. Large grid scenario: (**a**) Power Flows of Node 2 for Winter Case 9. (**b**)Power Flows of Node 6 for Winter Case 9.

Regarding BESS use, BESS is hardly used in Node 2. This can be explained intuitively as follows. The BESS is constrained to have a similar SOC at the beginning and the end of the day. Hence, the amount with which it is charged during the day (e.g. during the low energy price periods) needs to be discharged during the high energy price periods. However, if during the high energy price periods, there is needed power demand for the loads and the BESS capacity is not enough to cover them, then the node needs to import grid power and cannot discharge the BESS energy to the main grid for revenues. Therefore, the high amount of loads in a large grid also decreases the use of BESS, because it is preferred to use the low energy price time periods to import power for the needs of the node rather than use them to discharge the BESS to the grid for revenues. This is also validated in Figure 6 (b), which shows the respective power flows for Node 6 (only 6 buildings and 6 EV chargers), where BESS is considerably more utilized. Hence, it is concluded that the need for BESS is decreased when the grid size is increased.

6.2.2. Power Control Cost Comparison

The daily energy cost for all nodes 1-13 and cases 7-12 is shown in Figure 7. As in the small grid scenario, the influence of the seasonal effect is considered the most important since, for most nodes, Summer cases are characterized by a lower total cost. Moreover, the total node cost always results in equal or lower values when the BESS is used, and as a consequence, Cases 9 and 10 are always less costly than their respective Cases 7 and 8. Moreover, Cases 8 and 10, the Summer BESS cases without degradation, show the lowest total cost for almost every node. Furthermore, using BESS also closes the gap with the other cases, thus reducing the cost difference between cases with other characteristics and influencing factors. Finally, battery degradation also affects the total cost, with Cases 9 and 10 always resulting in a lower cost than their respective Cases 11 and 12. However, in some nodes, such as

Preprints.org (www.preprints.org) | NOT PEER-REVIEWED | Posted: 16 June 2026 doi:10.20944/preprints202606.1277.v1

Nodes 1 and 2, the contribution of the BESS for cost decrease is higher than the impact of degradation; hence, Case 7 results as the most costly case for these nodes. Nevertheless, in most of the nodes, the degradation cost is more significant, and Case 11 is the most costly case.

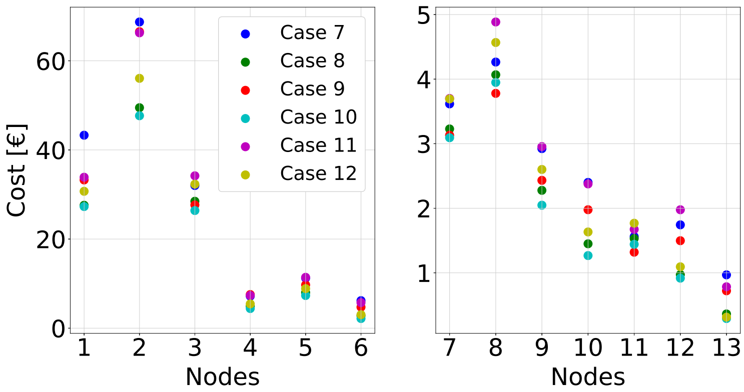

Figure 7. Daily Energy Cost for Nodes 1-13 and Cases 7-12.

6.2.3. V2G Energy Comparison

Figure 8 depicts on the left the total V2G energy used in the grid for all cases, while the node V2G energy used is shown for the big-level nodes (1, 2, 3) and medium-level nodes (4, 5, 6) with two heatmaps on the right. As explained, V2G is more likely to be used during Winter (Cases 7, 9, 11) due to lower PV availability, reaching up to 100kWh for Case 7. Moreover, introducing BESS in Cases 9-12 decreases the use of V2G since BESS is preferred due to lower power losses. Furthermore, considering battery degradation decreases V2G use further (Cases 11-12). Cases 7 and 9 are characterized by the highest V2G use, also in the heatmaps. Comparing Figure 8 with Figure 5(b), where V2G was only used in Case 1 and slightly in Case 3, V2G is used in all cases for the large grid and is never zero. This is because a grid of a larger size is more favorable for V2G energy use. The heatmaps also show that, excluding Node 6, larger Nodes 1-3 with a higher amount of loads, have more flexibility to use V2G in all cases.

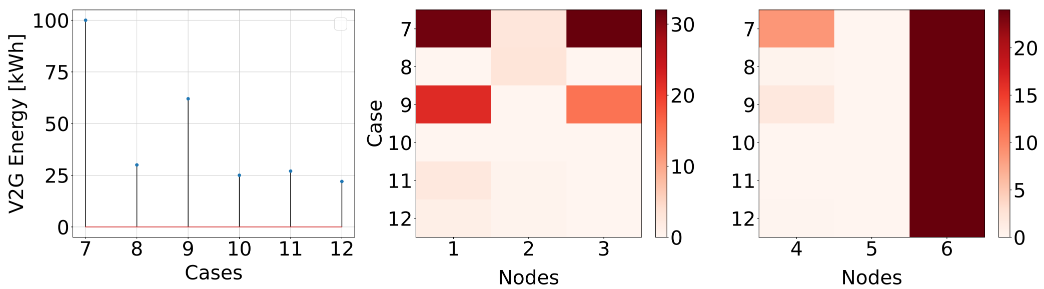

Figure 8. Total V2G Energy (left) & Node V2G Energy for Nodes 1-3 (center) and Nodes 4-6 (right) for Cases 7-12.

6.2.4. Grid Power Exchange Comparison

Finally, Table 8 summarizes the amounts of imported (Imp.) and exported (Exp.) energy for all the Nodes 1-6 and Cases 7-12. The imported energy greatly increases for the Winter cases (150% higher for Node 1 in Case 7 than in Case 8), while the use of BESS increases imported and exported amounts at most nodes (Cases 9 and 10 compared to Cases 7 and 8) to use its flexibility for revenues. Moreover, the exported energy amounts are increased for all nodes in Summer Case 8 compared to Winter Case 7 due to the higher PV generation (e.g. 270% for node 3). Finally, comparing the degradation cases 11 and 12 with their respective cases 9 and 10, the consideration of degradation decreases the imported and exported energy amounts for the smaller nodes; however, this is not always the case for Nodes 1-3. Therefore, in larger-size nodes with a larger available BESS capacity, the power control prefers to use its BESS capacity for revenues to compensate for the degradation cost rather than decrease the BESS equivalent cycle.

Table 8. Imported Energy (Imp.) & Exported Energy (Exp.) in kWh: for Nodes 1-13, Cases 7-12.

	Case 7		Case 8		Case 9		Case 10		Case 11		Case 12	
N.	**Imp.**	**Exp.**	**Imp.**	**Exp.**	**Imp.**	**Exp.**	**Imp.**	**Exp.**	**Imp.**	**Exp.**	**Imp.**	**Exp.**
1	1203.99	46.7	524.48	46.28	1647.39	487.7	527.44	55.11	927.19	73.7	644.7	180.48
2	1897.15	26.7	938.6	71.28	1864.21	43.83	924.09	88.44	2073.25	277.12	1066.84	210.47
3	889.28	13.2	517.47	27.09	1125.8	249.24	589.39	101.56	1017.74	151.74	583.02	100.1
4	244.9	17.04	111.27	20.25	248.73	20.25	152.72	60.5	294.73	68.99	131.49	44.06
5	304.86	9.39	154.09	17.82	371.7	76.31	178.61	42.51	331.28	44.11	166.68	32.58
6	194.19	10.68	68.3	20.17	281.48	98.01	101.29	54.42	255.71	71.63	66.34	22.53

7. Discussion and Validation

7.1. Comparison with Power Control Works

7.1.1. MPC Works

MPC works use the concept of the moving horizon for their control strategies. MPC models, such as this work, handle uncertainties, triggering re-optimizations of the rolling control horizon upon realization of uncertain events. A similar adaptive MPC strategy was developed in the PV-EV-BESS control work in [41], where the new predicted model states are adapted at every re-optimization according to the new user preferences using a Kalman filter-based estimator. However, the modeling of various charging details, such as the CC-CV regions of the capacity degradation, was not included. MPC models that also incorporate HPs and building heating can be found in the building EMS of [27], while EVs were also added in [40]. In [40], re-optimizations are triggered at every timestep, where the new user preferences and forecasted data are fed to the mode; consequently, the control horizon moves a period T forward. While re-optimizations at every timestep provide the highest protection against uncertainties, it can become very computationally expensive if the control horizon is too long or the selected timestep is too low. The MPC models in [26,27,40] remained MILP because they considered a steady COP; thus, the rated HP COP, the average COP over the horizon, and an approximation of the ideal COP, respectively. In this work, all cases were re-simulated with average COPS and MILP formulation (3.4 and 6 for Winter and Summer), finding an accuracy error increase up to 10% and computational time decrease up to 15%. On the contrary, while a variable temperature-dependent COP was considered in the building-level MPC PV-HP-TES control work in [35], the HP was ON-OFF and could deliver only zero or rated heating output. In this work, the variable COP, dictated in (26), makes (28) quadratic, and the control model MIQP. Hence, the model accuracy is increased at the expense of computational burden.

7.1.2. Multi-Objective Power Control Works

There are multiple ways to solve optimization problems with multiple objectives. Rule-based strategies can be developed that adjust with rules the priority of the objectives according to the dynamic state of the problem (e.g. temperature, SOC, PV generation, load in [37]). However, these rule-based logics can become extremely complex with multiple rules and cannot find the global optima. Nash bargaining models, such as in [42], construct different subproblems for every objective and search for Pareto optimal solutions; however, they can become computationally heavy with more than two objectives. Integrating all objectives (e.g., cost, thermal comfort, emissions, etc.) with different weights in the objective, such as in [36], eliminates the computational expense of the previous methods and adjusts priorities deliberately; however, they depend on the proper weight selection. Finally, translating all objectives into one in the objective function, such as in [11,53], and this work, transforms the problem into a a single simple optimization. However, it has the limitation that the objective priority depends on the resulting cost and is hardly altered.

Preprints.org (www.preprints.org) | NOT PEER-REVIEWED | Posted: 16 June 2026 doi:10.20944/preprints202606.1277.v1

7.2. Validation

7.2.1. Power Control Model

The power control model has been validated against a rule-based uncontrolled benchmark model based on [4,46] to show the cost reduction due to control, and the MPC EV smart-charging (SC) model in [53] to show its performance against other control works. The benchmark model has been created with the uncontrolled building heating model in [46], which operates the HPs only according to the desired building temperature interval [21°, 23°], and with the uncontrolled EV charging model in [4], which charges the EV fleets with rated power as soon as they arrive. It maximizes PV self-consumption according to the rule logic:

1) When the PV generation is higher than the total load, all the load is covered by the PV generation, and the rest of the PV power is exported to the main grid for revenues.

2) When the total load is higher than the PV generation, all PV generation is used for its cover, and the rest is covered by imported grid power.

The MPC model in [53] performs EV charging with minimum cost and maximum self-consumption. Due to the extra features of this work, such as HP heating, the specific cost metric C_{sp} in (46) has been used for the comparison (total cost C divided by the total exchanged grid power).

$$C_{sp} = \frac{C}{\sum_{t=1}^{T}(P_{im}^{t} - P_{ex}^{t})} \tag{46}$$

In Figure 9, the power flows of the uncontrolled, EV smart charging, and power control models are depicted. As seen, the low energy prices during [00:00, 06:00] are not taken advantage of in the uncontrolled model as they are in the power control model. Moreover, the EVs arrive during the energy price peak during [18:00, 20:00] and start charging immediately without avoiding the price peak, such as in the power control. Finally, the power scheduling of the EV smart charging and power control models is similar except for the addition of building heating. Moreover, Figure 10 depicts the comparison of Nodes 1 and 2 for Winter and Summer between the uncontrolled model and the power control model with and without BESS use concerning total cost and maximum needed power capacity (left plot). It can be seen that for all cases the cost is lower for the power control model, while, in most of them, a lower power capacity is also needed. In two cases, for Node 2 during Summer and Winter, a higher power capacity was needed for the power control model using BESS: 32kW and 33kW compared to 16kW and 20kW for the uncontrolled, respectively. Hence, a sensitivity analysis was realized for the power limits of these cases (right plot), proving that the power control model cost remains always lower when the same power limits are used. Finally, Table 9 summarizes the cost comparison of the power control and the EV SC models. The cost is highly reduced, especially when a BESS is used, reaching up to 30.6% reduction. Without the use of BESS, the specific cost of the power control model is slightly lower (up to 5.81%), which is due to the capability of V2G use.

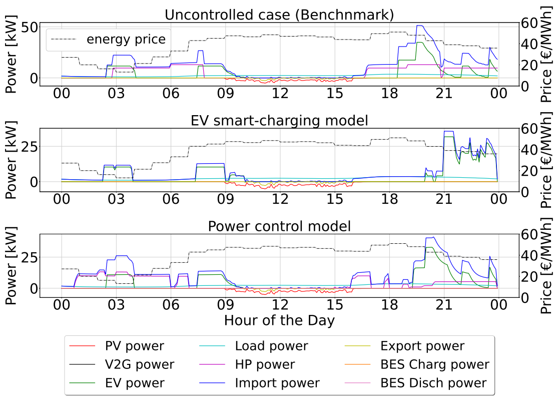

Figure 9. Comparison of power flows for the benchmark, EV SC [53], and power control algorithms: Node 1 - Winter.

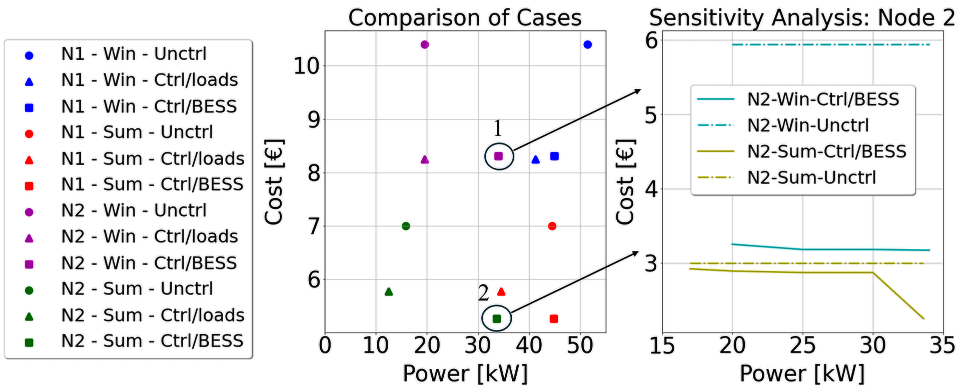

Figure 10. Total cost and maximum used power comparison between power control and benchmark model (Unctrl) for nodes N1-3 (left plot) & Sensitivity analysis of power limits for the two specific cases (right plot).

Table 9. Comparison of specific cost (€/kW) for EV SC and PCS, Nodes: N1 & N2, Winter - Summer.

Models	**Winter**		**Summer**	
	N1	**N2**	**N1**	**N2**
Model in [53]	3.05	3.24	4.59	4.76
Ctrl: No BESS	2.9: -4.83%	3.07: -5.25%	4.62: +0.74%	4.49: -5.81%
Ctrl: BESS	2.95: -3.09%	2.25: -30.6%	4.24: -7.56%	3.81: -20.11%

7.2.2. Battery Degradation Model

Validation of the original battery degradation model using experimental data has already been realized in [48] under various tests, such as storage, CC cycle, CC-CV cycle, and application-based dynamic current profile tests, founding a capacity loss error below 1% of the original capacity while the maximum relative error was below 21%.

For the validation of the linearized model, the real battery degradation has been calculated post-optimization and compared with the linear battery degradation results. Figure 11(a) depicts the real and linear cyclic degradation mechanisms (Qcyc 1 and Qcyc 2) and the total degradation Qcyc total for the BESS of Node 1. Moreover, the simultaneous BESS SOC and charging and discharging currents are depicted in Figure 11(b). The resulting root-mean-squared error (RMSE) values are $(1.9856, 1.8346, 2.0652) * 10^{-6}$ for Nodes 1-3, respectively, proving the accuracy of the developed linearized degradation model. Finally, the model's accuracy has been validated with the models in [48,54] under 9 conditions, and the results are summarized in Table 10, showing an accuracy error $< 3\%$ in most cases and no higher than 14%. The conditions are described below:

1) Simulation Time (ST): 1 year (y), Battery's year of life (YoL) 1$^{\text{st}}$, Min aging.
2) ST: 1y, YoL: ST, Min aging and avg SOC.
3) ST: 1y, YoL: ST, Min aging and throughput (TP).
4) ST: 1y, YoL: ST, Min aging, avg SOC, and TP.
5) ST: 9y, YoL: 1$^{\text{st}}$, Min aging.
6) ST: 9y, YoL: 10$^{\text{th}}$, Min aging.
7) ST: 9y, YoL: ST, Min aging and avg SOC.
8) ST: 9y, YoL: ST, Min aging and TP.

Preprints.org (www.preprints.org) | NOT PEER-REVIEWED | Posted: 16 June 2026 doi:10.20944/preprints202606.1277.v1

9) ST: 9y, YoL: ST, Min aging, avg SOC, and TP.

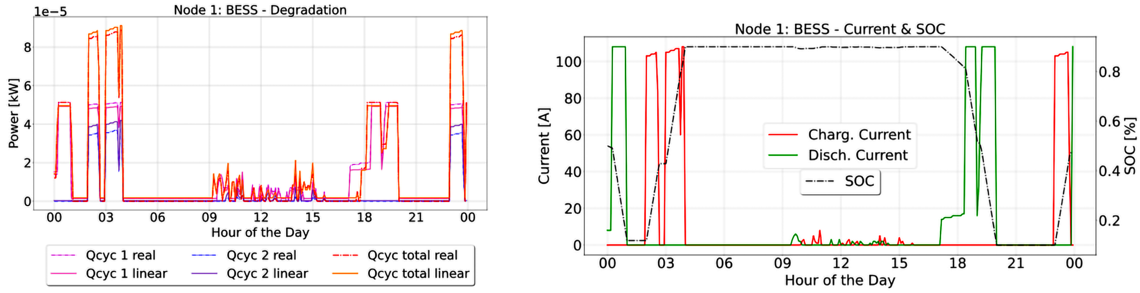

(a) (b)

Figure 11. Battery degradation: (**a**) Real and linearized cyclic battery degradation mechanisms in and post optimization (**b**)Charging/discharging battery current & SOC.

Table 10. Further validation of linearized battery degradation model.

	Model [48]			**Model [54]**		
Conditions	**Calendar**	**Cyclic**	**Total**	**Calendar**	**Cyclic**	**Total**
Condition 1	1.78%	0.67%	2.44%	1.35%	0.45%	1.8%
Condition 2	1.52%	0.79%	2.32%	1.29%	0.51%	1.8%
Condition 3	3.11%	0.74%	3.85%	1.75%	0.49%	2.23%
Condition 4	1.95%	0.76%	2.71%	1.38%	0.48%	1.86%
Condition 5	5.32%	1.96%	7.28%	10.48%	1.5%	11.98%
Condition 6	7.27%	2.15%	9.42%	11.31%	1.7%	13%
Condition 7	4.55%	2.36%	6.91%	10.06%	1.69%	11.75%
Condition 8	9.26%	2.24%	11.5%	12.1%	1.64%	13.73%
Condition 9	5.82%	2.15%	7.97%	10.68%	1.61%	12.29%

8. Conclusions

In this work, a two-level MIQP power control model is developed for the day-ahead and real-time scheduling of PVs, EVs, HPs, and BESS for energy arbitrage respecting the grid limits. The power control has been tested with and without BESS use under various conditions (seasons, grid types and sizes, and battery degradation). An important finding is that while V2G is less used than the BESS in small grids due to higher power losses, opposite trends are observed in larger grids with a vast amount of loads; hence, the importance of BESS decreases while the grid size increases. Moreover, the grid type also has a notable impact on the flexibility of the node since commercial grids import much less grid power and use less V2G due to lower flexibility. Another important finding is that while degradation costs are much lower than the power control costs, they become comparable in larger grids and can significantly alter the energy arbitrage decisions. Finally, the model has been compared and validated against other benchmark and control models, showing cost reductions of up to 5.81% and 30.6%, without and with BESS use, respectively.

In future work, considering more uncertainties (PV generation, weather data, load demand) is proposed to qualify the uncertainty management of the real-time scheduling level. Moreover, a weekly simulation is proposed to capture the intra-week effects. Finally, the dependence of the charger efficiencies on the power levels should be studied, which is expected to have a notable impact on the optimization decision-making.

Author Contributions: N.D: conceptualization, methodology, software, validation, investigation, data curation, visualization, writing—original draft preparation, writing—review and editing. G.R.C.M: funding acquisition,

 doi:10.20944/preprints202606.1277.v1

project administration, supervision, resources, writing—review and editing. P.B: funding acquisition, project administration. All authors have read and agreed to the published version of the manuscript.

Funding: This research was funded by the Dutch Research Council (NWO) as part of the ongoing research project NEON with project number 17628 of the research program Crossover

Data Availability Statement: The input and output data of this study are uploaded to the TU Delft repository https://repository.tudelft.nl/. Due to confidentiality reasons, some data are not publicly available, such as the distribution grids, scquired by Enerxis Groep operator. Data may be available from the authors upon reasonable request.

Acknowledgments: The authors gratefully acknowledge Enexis Groep for the acquisition of the used distribution grid, and Alvaro Menendez Agudin for the validation of the developed battery degradation model in other existing works.

Conflicts of Interest: The authors declare no conflicts of interest. The funders had no role in the design of the study; in the collection, analyses, or interpretation of data; in the writing of the manuscript; or in the decision to publish the results.

Abbreviations

The following abbreviations are used in this manuscript:

B/HEMS	Building/Home Energy Management System
B/TESS	Battery/Thermal Energy Storage System
CC-CV	Constant-current - Constant-voltage
COP	Coefficient of Performance
CvaR	Conditional Value at Risk
DA(M)	Day-ahead (Market)
DC	Direct Current
DER	Distributed Energy Resources
DG	Distribution Grid
DHW	Domestic Hot Water
DR	Demand Response
DSM	Demand Side Management
DSO	Distribution System Operator
DOD	Depth of Discharge
EV	Electric Vehicle
HH	Household
HP	Heat Pump
LCT	Low-carbon Technology
LFP	Lithium Ferrophosphate Battery
LIB	Lithium-Ion Battery
LV	Low Voltage
MDP	Markov Decision Process
MI(L/Q)P	Mixed-integer (Linear/Quadratic) Programming
MPC	Model Predictive Control
PDF	Probability Distribution Function
PV	Photovoltaics
RES	Renewable Energy Sources
RHO	Rolling Horizon Optimization
RMSE	Root-mean-squared Error
SC	Smart Charging
SHGC	Solar Heat Gain Coefficient
SOC	State of Charge
V2G	Vehicle-to-grid
WWR	Window-to-wall Ratio

References

1. Mohammad, A.; Zamora, R.; Lie, T.T. Transactive Energy Management of PV-Based EV Integrated Parking Lots. *IEEE Systems Journal* **2021**, *15*, 5674–5682. https://doi.org/10.1109/JSYST.2020.3043327.
2. Arnaudo, M.; Topel, M.; Laumert, B. Vehicle-To-Grid for Peak Shaving to Unlock the Integration of Distributed Heat Pumps in a Swedish Neighborhood. *Energies* **2020**, *13*. https://doi.org/10.3390/en13071705.
3. Agency, E.E. Greenhouse Gas Emissions by Source Sector, EU, 2022, 2023. https://ec.europa.eu/eurostat/statistics-explained/ [Accessed: (2025-07-09)].
4. Damianakis, N.; Mouli, G.R.C.; Bauer, P.; Yu, Y. Assessing the grid impact of Electric Vehicles, Heat Pumps & PV generation in Dutch LV distribution grids. *Applied Energy* **2023**, *352*, 121878. https://doi.org/https://doi.org/10.1016/j.apenergy.2023.121878.
5. Brinkel, N.; Gerritsma, M.; AlSkaif, T.; Lampropoulos, I.; van Voorden, A.; Fidder, H.; van Sark, W. Impact of rapid PV fluctuations on power quality in the low-voltage grid and mitigation strategies using electric vehicles. *International Journal of Electrical Power & Energy Systems* **2020**, *118*, 105741. https://doi.org/https://doi.org/10.1016/j.ijepes.2019.105741.
6. Giordano, F.; Ciocia, A.; Leo, P.D.; Mazza, A.; Spertino, F.; Tenconi, A.; Vaschetto, S. Vehicle-to-Home Usage Scenarios for Self-Consumption Improvement of a Residential Prosumer With Photovoltaic Roof. *IEEE Transactions on Industry Applications* **2020**, *56*, 2945–2956. https://doi.org/10.1109/TIA.2020.2978047.
7. Hu, J.; Zhou, H.; Li, Y.; Hou, P.; Yang, G. Multi-time Scale Energy Management Strategy of Aggregator Characterized by Photovoltaic Generation and Electric Vehicles. *Journal of Modern Power Systems and Clean Energy* **2020**, *8*, 727–736. https://doi.org/10.35833/MPCE.2019.000464.
8. Behi, B.; Baniasadi, A.; Arefi, A.; Gorjy, A.; Jennings, P.; Pivrikas, A. Cost–Benefit Analysis of a Virtual Power Plant Including Solar PV, Flow Battery, Heat Pump, and Demand Management: A Western Australian Case Study. *Energies* **2020**, *13*. https://doi.org/10.3390/en13102614.
9. Damianakis, N.; Yu, Y.; Mouli, G.C.R.; Bauer, P. Frequency Regulation Reserves Provision in EV Smart-Charging. In Proceedings of the 2023 IEEE Transportation Electrification Conference & Expo (ITEC), 2023, pp. 1–6. https://doi.org/10.1109/ITEC55900.2023.10187114.
10. Huang, S.; Wu, Q. Dynamic Tariff-Subsidy Method for PV and V2G Congestion Management in Distribution Networks. *IEEE Transactions on Smart Grid* **2019**, *10*, 5851–5860. https://doi.org/10.1109/TSG.2019.2892302.
11. Vermeer, W.; Mouli, G.R.C.; Bauer, P. Optimal Sizing and Control of a PV-EV-BES Charging System Including Primary Frequency Control and Component Degradation. *IEEE Open Journal of the Industrial Electronics Society* **2022**, *3*, 236–251. https://doi.org/10.1109/OJIES.2022.3161091.
12. Abdelaal, G.; Gilany, M.I.; Elshahed, M.; Sharaf, H.M.; El'gharably, A. Integration of Electric Vehicles in Home Energy Management Considering Urgent Charging and Battery Degradation. *IEEE Access* **2021**, *9*, 47713–47730. https://doi.org/10.1109/ACCESS.2021.3068421.
13. Aljohani, T.M.; Ebrahim, A.F.; Mohammed, O.A. Dynamic Real-Time Pricing Mechanism for Electric Vehicles Charging Considering Optimal Microgrids Energy Management System. *IEEE Transactions on Industry Applications* **2021**, *57*, 5372–5381. https://doi.org/10.1109/TIA.2021.3099083.
14. Cheng, R.; Cheng, W.; Li, J.; Chen, Z.; Shi, J.; Pan, Z.; Wu, Y.; Yu, T. Stochastic Dynamic Programming-Based Online Algorithm for Energy Management of Integrated Energy Buildings With Electric Vehicles and Flexible Thermal Loads. *IEEE Access* **2021**, *9*, 58780–58789. https://doi.org/10.1109/ACCESS.2021.3069278.
15. Carli, R.; Cavone, G.; Pippia, T.; De Schutter, B.; Dotoli, M. Robust Optimal Control for Demand Side Management of Multi-Carrier Microgrids. *IEEE Transactions on Automation Science and Engineering* **2022**, *19*, 1338–1351. https://doi.org/10.1109/TASE.2022.3148856.
16. Wang, B.; Dehghanian, P.; Zhao, D. Chance-Constrained Energy Management System for Power Grids With High Proliferation of Renewables and Electric Vehicles. *IEEE Transactions on Smart Grid* **2020**, *11*, 2324–2336. https://doi.org/10.1109/TSG.2019.2951797.
17. Sangswang, A.; Konghirun, M. Optimal Strategies in Home Energy Management System Integrating Solar Power, Energy Storage, and Vehicle-to-Grid for Grid Support and Energy Efficiency. *IEEE Transactions on Industry Applications* **2020**, *56*, 5716–5728. https://doi.org/10.1109/TIA.2020.2991652.
18. Foroozandeh, Z.; Ramos, S.; Soares, J.; Vale, Z. Goal Programming Approach for Energy Management of Smart Building. *IEEE Access* **2022**, *10*, 25341–25348. https://doi.org/10.1109/ACCESS.2022.3153341.
19. Imran, A.; Hafeez, G.; Khan, I.; Usman, M.; Shafiq, Z.; Qazi, A.B.; Khalid, A.; Thoben, K.D. Heuristic-Based Programable Controller for Efficient Energy Management Under Renewable Energy Sources and Energy

Storage System in Smart Grid. *IEEE Access* **2020**, *8*, 139587–139608. https://doi.org/10.1109/ACCESS.2020.3012735.
20. Roccotelli, M.; Mangini, A.M.; Fanti, M.P. Smart District Energy Management With Cooperative Microgrids. *IEEE Access* **2022**, *10*, 36311–36326. https://doi.org/10.1109/ACCESS.2022.3163724.
21. Lee, J.W.; Kim, M.K. An Evolutionary Game Theory-Based Optimal Scheduling Strategy for Multiagent Distribution Network Operation Considering Voltage Management. *IEEE Access* **2022**, *10*, 50227–50241. https://doi.org/10.1109/ACCESS.2022.3174077.
22. Çiçek, A.; Şengör, İ.; Güner, S.; Karakuş, F.; Erenoğlu, A.K.; Erdinç, O.; Shafie-Khah, M.; Catalão, J.P.S. Integrated Rail System and EV Parking Lot Operation With Regenerative Braking Energy, Energy Storage System and PV Availability. *IEEE Transactions on Smart Grid* **2022**, *13*, 3049–3058. https://doi.org/10.1109/TSG.2022.3163343.
23. Rafique, S.; Hossain, M.J.; Nizami, M.S.H.; Irshad, U.B.; Mukhopadhyay, S.C. Energy Management Systems for Residential Buildings With Electric Vehicles and Distributed Energy Resources. *IEEE Access* **2021**, *9*, 46997–47007. https://doi.org/10.1109/ACCESS.2021.3067950.
24. El-Taweel, N.A.; Farag, H.; Shaaban, M.F.; AlSharidah, M.E. Optimization Model for EV Charging Stations With PV Farm Transactive Energy. *IEEE Transactions on Industrial Informatics* **2022**, *18*, 4608–4621. https://doi.org/10.1109/TII.2021.3114276.
25. Zahedmanesh, A.; Muttaqi, K.M.; Sutanto, D. A Cooperative Energy Management in a Virtual Energy Hub of an Electric Transportation System Powered by PV Generation and Energy Storage. *IEEE Transactions on Transportation Electrification* **2021**, *7*, 1123–1133. https://doi.org/10.1109/TTE.2021.3055218.
26. D'Ettorre, F.; Conti, P.; Schito, E.; Testi, D. Model predictive control of a hybrid heat pump system and impact of the prediction horizon on cost-saving potential and optimal storage capacity. *Applied Thermal Engineering* **2019**, *148*, 524–535. https://doi.org/https://doi.org/10.1016/j.applthermaleng.2018.11.063.
27. Gelleschus, R.; Böttiger, M.; Bocklisch, T. Optimization-Based Control Concept with Feed-in and Demand Peak Shaving for a PV Battery Heat Pump Heat Storage System. *Energies* **2019**, *12*. https://doi.org/10.3390/en12112098.
28. Clift, D.; Suehrcke, H. Control optimization of PV powered electric storage and heat pump water heaters. *Solar Energy* **2021**, *226*, 489–500. https://doi.org/10.1016/j.solener.2021.08.059.
29. Vivian, J.; Prataviera, E.; Cunsolo, F.; Pau, M. Demand Side Management of a pool of air source heat pumps for space heating and domestic hot water production in a residential district. *Energy Conversion and Management* **2020**, *225*, 113457. https://doi.org/https://doi.org/10.1016/j.enconman.2020.113457.
30. Wakui, T.; Sawada, K.; Yokoyama, R.; Aki, H. Predictive management for energy supply networks using photovoltaics, heat pumps, and battery by two-stage stochastic programming and rule-based control. *Energy* **2019**, *179*, 1302–1319. https://doi.org/https://doi.org/10.1016/j.energy.2019.04.148.
31. Eggimann, S.; Hall, J.W.; Eyre, N. A high-resolution spatio-temporal energy demand simulation to explore the potential of heating demand side management with large-scale heat pump diffusion. *Applied Energy* **2019**, *236*, 997–1010. https://doi.org/https://doi.org/10.1016/j.apenergy.2018.12.052.
32. Valinejad, J.; Marzband, M.; Korkali, M.; Xu, Y.; Al-Sumaiti, A.S. Coalition Formation of Microgrids with Distributed Energy Resources and Energy Storage in Energy Market. *Journal of Modern Power Systems and Clean Energy* **2020**, *8*, 906–918. https://doi.org/10.35833/MPCE.2019.000116.
33. Good, N.; Mancarella, P. Flexibility in Multi-Energy Communities With Electrical and Thermal Storage: A Stochastic, Robust Approach for Multi-Service Demand Response. *IEEE Transactions on Smart Grid* **2019**, *10*, 503–513. https://doi.org/10.1109/TSG.2017.2745559.
34. Violante, W.; Cañizares, C.A.; Trovato, M.A.; Forte, G. An Energy Management System for Isolated Microgrids With Thermal Energy Resources. *IEEE Transactions on Smart Grid* **2020**, *11*, 2880–2891. https://doi.org/10.1109/TSG.2020.2973321.
35. Gasser, J.; Cai, H.; Karagiannopoulos, S.; Heer, P.; Hug, G. Predictive energy management of residential buildings while self-reporting flexibility envelope. *Applied Energy* **2021**, *288*, 116653. https://doi.org/https://doi.org/10.1016/j.apenergy.2021.116653.
36. Athanasiadis, C.L.; Papadopoulos, T.A.; Kryonidis, G.C.; Doukas, D.I. A Holistic and Personalized Home Energy Management System With Non-Intrusive Load Monitoring. *IEEE Transactions on Consumer Electronics* **2024**, *70*, 6725–6737. https://doi.org/10.1109/TCE.2024.3483938.
37. Zhang, L.; Feng, G.; Huang, K.; Bi, Y.; Chang, S.; Li, A. Design and optimization for photovoltaic heat pump system integrating thermal energy storage and battery energy storage. *Energy and Buildings* **2025**, *329*, 115277. https://doi.org/https://doi.org/10.1016/j.enbuild.2025.115277.

 doi:10.20944/preprints202606.1277.v1

38. Yousefi, M.; Hajizadeh, A.; Soltani, M.N.; Hredzak, B. Predictive Home Energy Management System With Photovoltaic Array, Heat Pump, and Plug-In Electric Vehicle. *IEEE Transactions on Industrial Informatics* **2021**, *17*, 430–440. https://doi.org/10.1109/TII.2020.2971530.
39. Vermeer, W.; Chandra Mouli, G.R.; Bauer, P. Real-Time Building Smart Charging System Based on PV Forecast and Li-Ion Battery Degradation. *Energies* **2020**, *13*. https://doi.org/10.3390/en13133415.
40. Fotouhi Ghazvini, M.A.; Antoniadou-Plytaria, K.; Steen, D.; Tuan, L.A. Two-stage demand-side management in energy flexible residential buildings. *The Journal of Engineering* **2024**, *2024*, e12372, [https://ietresearch.onlinelibrary.wiley.com/doi/pdf/10.1049/tje2.12372]. https://doi.org/https://doi.org/10.1049/tje2.12372.
41. Sen, S.; Kumar, M. Distributed-MPC Type Optimal EMS for Renewables and EVs Based Grid-Connected Building Integrated Microgrid. *IEEE Transactions on Industry Applications* **2024**, *60*, 2390–2408. https://doi.org/10.1109/TIA.2023.3332055.
42. Li, Y.; Wang, J.; Cao, Y. Multi-objective distributed robust cooperative optimization model of multiple integrated energy systems considering uncertainty of renewable energy and participation of electric vehicles. *Sustainable Cities and Society* **2024**, *104*, 105308. https://doi.org/https://doi.org/10.1016/j.scs.2024.105308.
43. Hosseini, S.M.; Carli, R.; Dotoli, M. Robust Optimal Energy Management of a Residential Microgrid Under Uncertainties on Demand and Renewable Power Generation. *IEEE Transactions on Automation Science and Engineering* **2021**, *18*, 618–637. https://doi.org/10.1109/TASE.2020.2986269.
44. Huang, P.; Lovati, M.; Zhang, X.; Bales, C.; Hallbeck, S.; Becker, A.; Bergqvist, H.; Hedberg, J.; Maturi, L. Transforming a residential building cluster into electricity prosumers in Sweden: Optimal design of a coupled PV-heat pump-thermal storage-electric vehicle system. *Applied Energy* **2019**, *255*, 113864. https://doi.org/https://doi.org/10.1016/j.apenergy.2019.113864.
45. Damianakis, N.; Mouli, G.R.C.; Yu, Y.; Bauer, P. Coordinated Power Control of PV Generation, Electric Mobility and Electric Heating in Different Grids. In Proceedings of the 2024 IEEE 10th International Power Electronics and Motion Control Conference (IPEMC2024-ECCE Asia), 2024, pp. 2082–2087. https://doi.org/10.1109/IPEMC-ECCEAsia60879.2024.10567854.
46. Damianakis, N.; Chandra Mouli, G.R.; Bauer, P. Risk-averse Estimation of Electric Heat Pump Power Consumption. 06 2023, pp. 1–6. https://doi.org/10.1109/CPE-POWERENG58103.2023.10227424.
47. Oliyide, R.O.; Cipcigan, L.M. The impacts of electric vehicles and heat pumps load profiles on low voltage distribution networks in Great Britain by 2050 **2021**. *11*, 30–45. https://doi.org/10.25081/imrj.2021.v11.7308.
48. Schimpe, M.; von Kuepach, M.E.; Naumann, M.; Hesse, H.C.; Smith, K.; Jossen, A. Comprehensive Modeling of Temperature-Dependent Degradation Mechanisms in Lithium Iron Phosphate Batteries. *Journal of The Electrochemical Society* **2018**, *165*, A181. https://doi.org/10.1149/2.1181714jes.
49. Battery Report. Technical report, Volta Foundation, 2024.
50. Consumption Profiles 2021.
51. Worldwide irradiation data.
52. Central collection and publication of electricity generation, transportation and consumption data and information for the pan-European market.
53. Yu, Y.; De Herdt, L.; Shekhar, A.; Mouli, G.R.C.; Bauer, P. EV Smart Charging in Distribution Grids–Experimental Evaluation Using Hardware in the Loop Setup. *IEEE Open Journal of the Industrial Electronics Society* **2024**, *5*, 13–27. https://doi.org/10.1109/OJIES.2024.3352265.
54. Petit, M.; Prada, E.; Sauvant-Moynot, V. Development of an empirical aging model for Li-ion batteries and application to assess the impact of Vehicle-to-Grid strategies on battery lifetime. *Applied Energy* **2016**, *172*, 398–407. https://doi.org/https://doi.org/10.1016/j.apenergy.2016.03.119.